

Universidad de Cantabria

Departamento de Física Moderna

CSIC - Universidad de Cantabria

Instituto de Física de Cantabria

**Detection of Point Sources in Maps of the
Cosmic Microwave Background Radiation
by means of Optimal Filters**

A dissertation submitted in partial of the requirements

for the degree of Doctor of Philosophy in Physics

by

Marcos López-Caniego Alcarria

2006

Introduction

1.1 The Cosmic Microwave Background Radiation

1.1.1 Introduction

In the last decade an increasing number of experiments have produced important results in the field of cosmology, allowing for a better understanding and characterization of the cosmological model of the universe. The “Concordance Model”, the current model of Big Bang cosmology, is based on the theory of inflation and on the Λ -CDM model, that includes cold dark matter (CDM) and a cosmological constant. The theory of inflation predicts a nearly scale-invariant spectrum of primordial density perturbations, homogeneity and isotropy on the largest scales, a universe without spatial curvature and Gaussianity of the density fluctuations. This simple model is supported by the observations of the cosmic microwave background radiation (CMB), the accelerating expansion of the universe measured with distant supernovae and the large scale structure of the universe. The “cold dark matter”, non-baryonic weakly interacting matter, accounts for 26% of the energy density in the universe. The baryonic matter accounts for an additional 4% that makes up the atoms. The remaining 70% is the “dark energy”, with an equation of state close to a cosmological constant, that allows for the current accelerating expansion of the universe. In particular, data from the experiments dedicated to the study of the CMB radiation have contributed to the determination with unprecedented precision of the cosmological parameters that characterize this model. The CMB radiation is a relic radiation from the Big Bang that has traveled through the space time for ~ 14 thousand million years. The mere existence of this radiation and its precise measurement strongly supports the theory of the Big Bang. Moreover, imprinted in this radiation is information about the early universe when it was only approximately 375.000 years old.

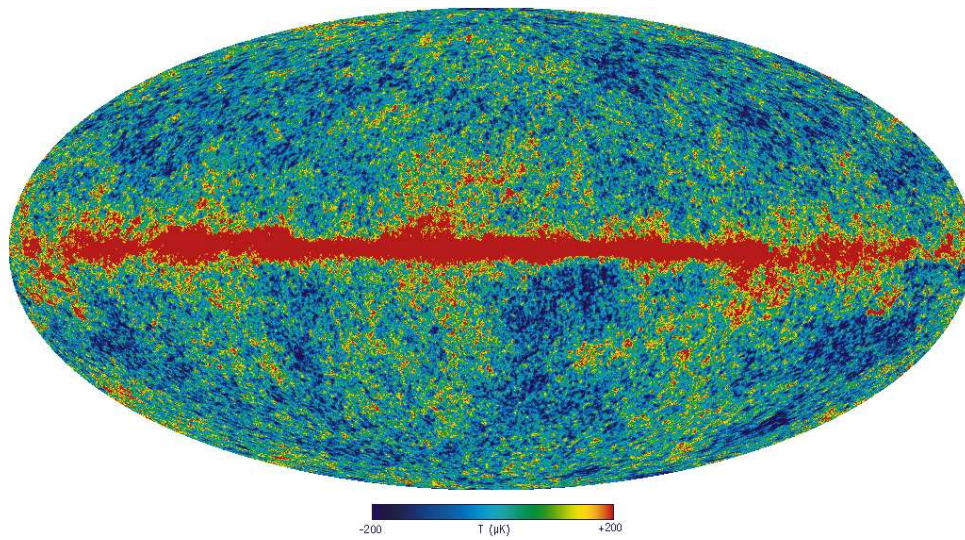


Figure 1.1 This image shows a full-sky map of the cosmic microwave background anisotropy and foreground signal from our Galaxy (mainly concentrated in the central red band) for the 94 GHz channel of the WMAP satellite third year data release [73].

1.1.2 Origins of the CMB

Some 14 thousand million years ago the universe was born in a big explosion known as the Big Bang. At that time the universe was made of a very hot plasma, a mixture of very energetic photons continuously interacting with electrons and baryons, preventing these from forming atoms. Then the universe expanded for almost 375.000 years and cooled to 3000 Celsius degrees, the protons and electrons came together to form atoms and the photons, for the first time, were no longer scattered by collisions with charged particles, and continued their journey through the space. The period of time when this process took place is known as the epoch of decoupling. When this happened, different regions had slightly different temperatures, depending on their initial conditions at the time when decoupling started. In general, these photons have preserved their relative temperature differences, and this produces the pattern of hotter and colder regions in the microwave sky (see figure 1.1).

Nowadays, photons coming from all directions with a temperature of $\sim 2.725 \pm 0.001$ Kelvin form the CMB radiation [99]. This radiation was first detected back in 1964 by Arno Penzias and Robert Wilson of *AT&T* Bell Laboratories, in Holmdel, New Jersey with an antenna originally used for satellite communications. They found an excess radio noise that seemed to be independent of the direction where the antenna was

pointing, which in principle could give a hint of its non Galactic origin.

A decade before, George Gamow formulated the theory of the Big Bang, a theory that could explain how the atoms could have formed in a hot expanding universe. Gamow's collaborators, Ralph Alpher and Robert Herman, studied the thermal evolution of the universe and came to the conclusion that, in the present time, after thousands of millions of years of expansion, the temperature of the universe and that of the photons of this relic radiation must be of the order of 5 Kelvin. Although they had made a clear prediction of what the temperature of the universe had to be, they did not try to detect it.

It was not until 15 years later that scientists Robert Dicke in Princeton and Yakov Zel'dovich in Moscow rediscovered independently Gamow's theory. Dicke, Peebles, Roll and Wilkinson realized the great importance of the CMB radiation and decided to build an instrument to search for it at radio wavelengths. At that time they heard of Penzias and Wilson mysterious signal and, in a meeting between the Princeton and Holmdel groups, they determined that the antenna temperature was indeed due to the microwave background radiation. Both groups of scientists published their works simultaneously [36, 111]. Penzias and Wilson presented the details of their discovery while Dicke formulated the theoretical framework for the origin of the CMB. In the late 1970s Penzias and Wilson were awarded the Nobel prize for their discovery.

In the last decades the CMB radiation has been studied thoroughly and it has been found that this radiation is very uniform and isotropic all over the sky, roughly to 1 part in 100.000. If the radiation came from a source in the local universe it would be unevenly distributed throughout space, therefore, it is believed that its origin is cosmological. The intensity of this radiation has been measured at many wavelengths and it possesses the black-body spectrum characteristic of a system in perfect thermal equilibrium, at a time when the matter and radiation had the exact same temperature. Let us consider a box with such dense and opaque walls that there is no radiation exchange with the outside. The field of radiation of this box is characterized by the temperature of its walls and this kind of hypothetical perfect radiator/absorber at this temperature is known as blackbody. The cosmic microwave background radiation is the best known natural black body. In the early 1990s, NASA's COsmic Background Explorer (COBE) satellite carefully measured it using the Far-Infrared Absolute Spectrophotometer (FIRAS) instrument. The result of these measurements [99, 100] was the most precisely measured black body spectrum ever (see figure 1.2).

Moreover, in the early 1970s cosmologists such as Zel'dovich, Harrison, Peebles and Yu realized that the universe would have to have small inhomogeneities in the dis-

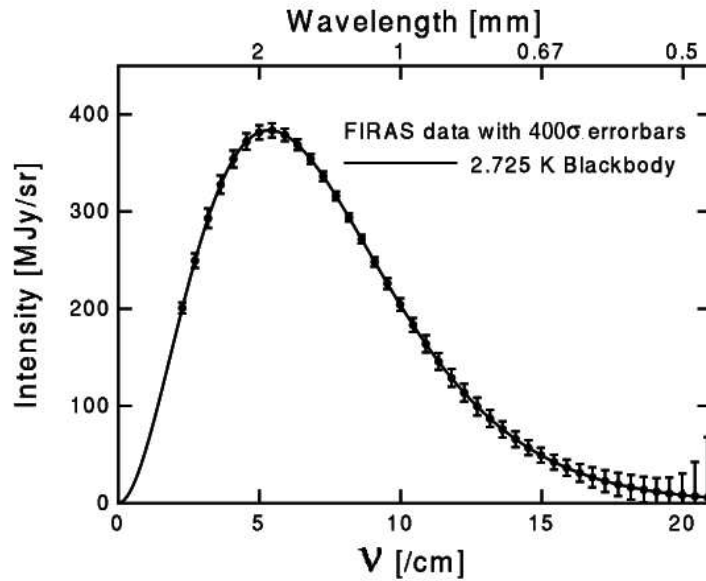


Figure 1.2 CMB frequency spectrum obtained with the FIRAS instrument on COBE in 1996. This spectrum corresponds to that of a black-body with temperature $T = 2.725 \pm 0.001$ K. The error bars have been multiplied by 400.

tribution of matter and Rashid Sunyaev realized that they would have an imprint in the CMB. These imprints were first detected by the Differential Microwave Radiometer (DMR) instrument on the COBE satellite and allowed to measure the approximate scale-invariant shape of the spectrum of density fluctuations [129]. This confirmed the theory of gravitational instability for the formation of large scale structure (LSS) and determined an initial spectrum of fluctuations characterized by density fluctuations with approximately equal amplitude when entering the horizon. The scientist G. Smoot, principal investigator of DMR, and J.C. Mather, principal investigator of FIRAS, received the Nobel price in 2006 for the contribution of COBE to physics and cosmology.

Following the results of COBE several ground and balloon-based experiments measured these anisotropies, departures of 1 part in 100.000 from the 2.73 Kelvin in the microwave background radiation. In the late 1990s several experiments, in particular BOOMERANG [28] and MAXIMA [64], determined that the curvature of the universe is close to zero, that is, the geometry is spatially flat. This result was confirmed in 2003 by NASA's satellite Wilkinson Anisotropy Probe (WMAP) [11].

1.1.3 Anisotropies of the CMB and Power Spectrum

The anisotropies of the CMB are the angular fluctuations in the intensity of the CMB radiation. In order to deal with these fluctuations in a statistical way, we may interpret them as a realization of a random field on the sphere. As we mentioned above, the spectral behavior of the CMB follows a blackbody of temperature 2.73 Kelvin, and we will consider the anisotropies as fluctuations in temperature with respect to it in different directions. These fluctuations of temperature on the surface of the sphere are a function of the spherical coordinates and the most appropriate way to deal with these fluctuations is expanding them in the orthogonal base of the spherical harmonics:

$$\frac{\Delta T}{T}(\theta, \phi) = \frac{T(\theta, \phi) - T_0}{T_0} = \sum_{\ell=1}^{\infty} \sum_{m=-\ell}^{\ell} a_{\ell m} Y_{\ell m}(\theta, \phi) \quad (1.1.1)$$

$$a_{\ell m} = \int_0^{2\pi} d\phi \int_0^{\pi} d\theta Y_{\ell m}^*(\theta, \phi) \frac{\Delta T}{T} \quad (1.1.2)$$

where θ and ϕ are the angular coordinates on the sphere and $a_{\ell m}$ represent the spherical harmonic coefficients. In this expansion the mode ℓ corresponds to an angular distance $\theta \sim \frac{180^\circ}{\ell}$, and therefore, low ℓ 's correspond to big angular distances, whereas high ℓ 's correspond to small scales. A detailed review of this topic can be found in Bond & Efstathiou [15], White, Scott, & Silk [152].

The temperature fluctuations of the CMB were originated by primordial quantum fluctuations at the epoch of inflation [59]. This theory predicts Gaussian initial quantum fluctuations and since $\Delta T/T$ is a linear combination of the latter, they will also follow a Gaussian distribution.

The correlation function of the temperature fluctuations is

$$C(\theta) = \left\langle \frac{\Delta T}{T}(\vec{\Omega}_1) \frac{\Delta T}{T}(\vec{\Omega}_2) \right\rangle = \sum_{\ell m} \sum_{\ell' m'} \langle a_{\ell m} a_{\ell' m'}^* \rangle Y_{\ell m}(\theta_1, \phi_1) Y_{\ell' m'}(\theta_2, \phi_2) \quad (1.1.3)$$

where $\vec{\Omega}_1$ and $\vec{\Omega}_2$ denote two unitary vectors pointing towards the two directions in the sky given by the coordinates (θ_1, ϕ_1) and (θ_2, ϕ_2) , and $\vec{\Omega}_1 \vec{\Omega}_2 = \cos(\theta)$. If the isotropy and homogeneity properties are verified, then the angular power spectrum C_ℓ can be written as

$$\langle a_{\ell m} a_{\ell' m'}^* \rangle = C_\ell \delta_{\ell \ell'} \delta_{m m'}, \quad (1.1.4)$$

where $\langle \cdot \rangle$ denotes averaging over sufficiently large volumes.

The correlation function of the temperature fluctuations, $C(\theta)$, is related to the angular power spectrum C_ℓ through the Legendre transform

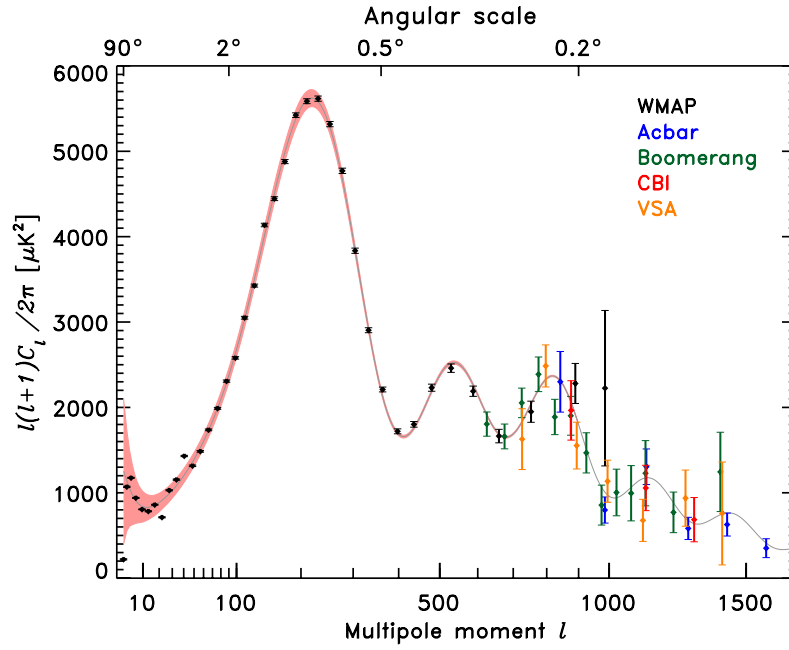


Figure 1.3 The WMAP three-year power spectrum (in black) and recent measurements of the CMB angular power spectrum with other experiments [73]. The band is the binned 1σ cosmic variance error.

$$C(\theta) = \sum_{\ell} \frac{2\ell+1}{4\pi} C_{\ell} P_{\ell}(\cos\theta) \quad (1.1.5)$$

where P_{ℓ} are the Legendre polynomials of order ℓ , and we have used the following property of the spherical harmonics

$$\sum_{m=-\ell}^{\ell} Y_{\ell m}(\theta_1, \phi_1) Y_{\ell m}^*(\theta_2, \phi_2) = \frac{2\ell+1}{4\pi} P_{\ell}(\cos\theta). \quad (1.1.6)$$

This expression for the correlation is independent of the direction, a sign of the isotropy of the field. In principle, both quantities $C(\theta)$ and C_{ℓ} are equivalent in the sense that they contain the same information. However, the null correlation of the C_{ℓ} 's for different values of ℓ makes it appropriate for this kind of studies, and we normally use it as $\ell(\ell+1)C_{\ell}/2\pi$, i.e. the power per logarithmic interval in ℓ for large ℓ , for $\ell \geq 2$. The case $\ell = 1$ is the dipole moment due to our own motion with respect to the CMB and is not considered because of its extrinsic origin. In figure (1.3) we show the angular power spectrum measured by the WMAP third year data [73] together with the measurements of other recent experiments

There is a limitation in the accuracy in the determination of the angular power spectrum C_ℓ due to the so-called “cosmic variance”, the error introduced by the fact that there is only one universe, and therefore, a single observable realization of the field of temperature fluctuations. For Gaussian temperature fluctuations, the “cosmic variance” can be easily calculated. For a given ℓ there are $(2\ell + 1) a_{\ell m}$ coefficients and from the dispersion of a chi-squared distribution with $2\ell + 1$ degrees of freedom we obtain

$$\Delta C_\ell = \frac{\sqrt{2}}{\sqrt{2\ell + 1}} C_\ell. \quad (1.1.7)$$

The cosmic variance is just one of the several sources of error that must be taken into account. It is important to know the fraction of the sky covered by the experiment as well as its sensitivity. Moreover, a very important source of error that must be taken into account arises from the fact that the field of temperature fluctuations can not be observed directly because there are several other components that are mixed with it and it is of great important to be able to separate these from the true underlying CMB temperature field. These “contaminants” can be diffuse galactic contributions (synchrotron, thermal dust and free-free emission), compact emissions (extragalactic point sources and clusters of galaxies) and a small contribution from weak gravitational lensing from the large scale structure.

The CMB anisotropies can be divided in two groups depending on their origin:

- **primary anisotropies**, which are due to effects that occurred at the last scattering surface and before, an epoch known as the period of recombination or decoupling because due to the expansion of the universe the temperature cooled, the radiation decoupled from the matter and the electrons and protons formed the first atoms.
- **secondary anisotropies**, which are due the interactions of the CMB photons with hot gas or gravitational potentials, between the last scattering surface and the observer

Their structure is determined by the following effects: Sachs-Wolfe effect, acoustic oscillations of the photon-baryon fluid and diffusion damping (also known as collisionless damping or Silk damping). Regarding the Sachs-Wolfe effect, it is the dominant effect on large scales, the most important of the different physical processes by which the primordial density fluctuations have left their imprint on the CMB radiation in the form of small variations in the temperature of this radiation in different directions on the sky. As for the acoustic oscillations, there is a competition between the radiation

pressure from the photons and the gravitational compression of the fluid into potential wells, which sets up acoustic oscillations in the fluid. At the time of decoupling all these oscillations stopped and the information of the phase in which they were just before that moment is preserved in the photons. Therefore, there will be a harmonic series of peaks in wavelength associated with the acoustic oscillations, and these peaks will contain important information about the shape of the universe, the amount of dark matter, baryon density, etc. The theory predicts the existence of the first acoustic peak between the angular scales 0.1° and 2° , and corresponds to the scales at which the acoustic oscillations of the photon-baryon fluid reached their maximum amplitude, i.e. an oscillation that compressed and rarefied the regions of plasma to the maximum extent at the time of recombination. The regions with the greatest variations in temperature subtend about 1° across the sky. The subsequent peaks correspond to the similar acoustic oscillations at other scales, although they were not at their maximum amplitude. The position of these peaks is determined by the geometry of the universe, because the same physical region subtends different angular scales depending on the curvature of the universe.

Regarding the diffuse damping at very small scales, due to the expansion of the universe the plasma rarefies, but the decoupling of matter and radiation is not instantaneous and the surface of last scattering has a finite thickness ($\Delta z \sim 100$, Jones & Wyse [81], where z is the redshift, the relative difference between the emitted and observed frequency of the photon). The fluctuations with angular sizes smaller than the thickness of the surface of last scattering have their amplitudes reduced due to the averaging produced between the photons coming from the inner side and those closer to the outer side of the surface. This contributes to the exponential suppression of anisotropies on small scales ($\theta \lesssim 10' \Omega^{1/2}$, where Ω is the ratio of the actual density of the universe and the critical density, turnover density between a closed and an open universe). These effects, the Sachs-Wolfe plateau at large scales and the harmonic series of peaks together with the exponential decay gives rise to the “angular power spectrum”, a representation of the amplitude of the fluctuations in temperature with angle (see figure 1.4).

Primary Anisotropies of the CMB

The primary anisotropies were produced before or during the recombination epoch. They can be produced by perturbations in the metric, intrinsic fluctuations and velocity contributions [97, 107, 152]. A general expression that takes into account these effects is

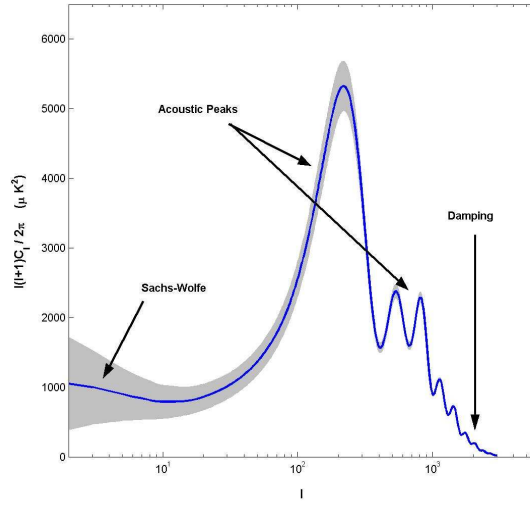


Figure 1.4 C_ℓ for the best fit model given in Bennett et al. [11]. The range of ℓ where the different physical effects dominate is indicated. The gray band involving the C_ℓ is the unavoidable error due to the cosmic variance. The spectrum has been computed using the CMBFAST code.

$$\frac{\Delta T}{T} = \vec{n} \cdot (\vec{v}_{ob} - \vec{v}_d) - \frac{1}{3} (\phi_{ob} - \phi_d) + \frac{1}{4} \delta_d^\gamma \quad (1.1.8)$$

where \vec{n} is the direction of observation and the subindex d denotes quantities at the time of decoupling and $c = 8\pi G \equiv 1$. These terms are model dependent and will characterize the anisotropies. Note that all these terms introduce angular dependencies in the temperature except for ϕ_{ob} .

1. **Doppler effect:** the first term in the previous equation $\vec{n} \cdot \vec{v}_{ob}$ corresponds to the Doppler shift produced by the motion of the observer with respect to the comoving coordinate system of the CMB. The shift towards the blue region of the spectrum will be observed in the direction of the motion and a red shift in the opposite direction. This effect is also called “dipole” because it contributes to the dipolar moment in the expansion in spherical harmonics of the temperature fluctuations field. This anisotropy was detected for the first time in 1975 [26] but it was not until 1996 that the COBE team measured its amplitude precisely: $3.372 \pm 0.007 mK$ [45]. There is an additional term $\vec{n} \cdot \vec{v}_d$ produced by the Doppler effect, although in this case it corresponds to the motion of the electrons with respect to the comoving system of the matter on the surface of last scattering.
2. **Sachs-Wolfe effect (SW):** this effect corresponds to the term $\frac{1}{3} (\phi_{ob} - \phi_d)$ in the

previous equation and it was formulated by Sachs & Wolfe [122]. It is the most important of the physical processes by which the primordial density fluctuations left their imprint on the CMB in the form of small variations in the temperature of this radiation in different directions on the sky. It has its origin in the gravitational potentials at the surface of last scattering, when the photons enter and then leave the potential well at the epoch of recombination, losing part of their energy and getting redshifted and then gaining it and getting blueshifted. This effect dominates at scales larger than the size of the horizon at the time of recombination, $\theta \gtrsim 2^\circ \Omega^{1/2}$. At these scales, the initial perturbations can not be affected by causal processes and, therefore, cosmic microwave anisotropies corresponding to these scales will be directly related to the fluctuations in the matter density power spectrum. The best fit to the matter power spectrum made by COBE [10] yielded an spectral index $n = 1.2 \pm 0.3$, compatible to the Harrison-Zeldovich spectrum ($n = 1$, scale-invariant power spectrum). The latest estimation from WMAP third year data is $n = 0.951 \pm 0.017$, and it is not compatible with the Harrison-Zeldovich spectrum above 2σ . This may be important when trying to detect the B mode of polarization.

3. **Intrinsic fluctuations:** before the epoch of recombination, when the matter and radiation were coupled, inhomogeneities in the matter density field induced fluctuations in the temperature field of the photons. Then, when matter and radiation decoupled, the photons were released preserving the information about the density fields in the surface of last scattering. In order to determine the fluctuations in the radiation density field, the last term in the previous equation $\frac{1}{4}\delta_d^\gamma$, a complicated system of coupled differential equations describing the evolution of the fluctuations in the radiation density field, baryonic matter and dark matter at the time of decoupling must be solved.

As mentioned above, there are several physical processes that reduce the amplitude of the fluctuations, mainly at smaller angular scales. One is related to the fact that the surface of last scattering has a finite thickness. Another of these mechanisms is the “Silk damping” [128]. The photons will travel from those regions with a higher density to those with a lower density through diffusion, dragging the electrons, that are coupled to the protons, with them via Compton interaction. This diffusion has the effect of damping out the fluctuations and is more important with decreasing size of the fluctuations, and it is expected that the peaks vanish for very small angular scales.

Secondary Anisotropies of the CMB

The secondary anisotropies are produced due to the interactions of the CMB photons between the last scattering surface and the observer. We will consider the following effects:

1. Gravitational Effects

Gravitational fields can induce secondary anisotropies in the CMB temperature field in different ways, e.g., through the integrated Sachs-Wolfe effect (ISW). In this case, when a photon falls in and climbs out of a potential well the net change in the energy of the photon is zero, as long as the depth of the well is constant. If the depth is changing, the blueshift of the photon from falling and its redshift from climbing out do not cancel. The magnitude of the ISW is given by:

$$\frac{\Delta T}{T} = \int \frac{\partial \phi}{\partial t}(\vec{r}, t) dt. \quad (1.1.9)$$

On the other hand, a gravitational field can also modify the trajectory of a photon without modifying its energy, an effect known as gravitational lensing. We can summarize the different cases that generate secondary anisotropies as follows:

- *Early ISW*: at the epoch of last scattering, when the universe is not completely matter dominated, the photon contribution to the density of the universe is not negligible and the decay in the potential shortly after the last scattering gives rise to this effect. The contribution of this effect to the angular power spectrum is at scales just larger than the first acoustic peak.
- *Late ISW*: In an open or Λ model, when the matter does not dominate the expansion, the universe enters a rapid expansion phase. As density fluctuations are frozen in, the potential again decays leading to an ISW effect.
- *Rees-Sciama*: At later times, evolving non-linear structures cause the potentials to vary with time. This kind of ISW effect is usually called the Rees-Sciama effect [117].
- *Gravitational lensing*: This effect is also produced by gravitational fields, as in the case of ISW effect, but can not change the energy of the photons, just their trajectory. This effect slightly distorts the image of the last scattering surface, producing a smearing of the angular power spectrum.
- *Gravitational waves*: this would affect the radiation power spectrum at scales larger than the horizon at recombination.

2. Scattering effects from reionization

The reionization of the universe after recombination produces free electrons that rescatter off the photons of the CMB radiation. Therefore, primary anisotropies are washed out and new secondary ones appear. If the universe becomes globally reionized at high redshift, primary anisotropies can be dramatically suppressed. On the other hand, local reionization also produces characteristic features in the CMB.

- If the universe becomes globally reionized at a given redshift z_r , a certain fraction of the CMB photons will be rescattered by free electrons. Therefore, a photon coming toward us from a particular direction, has not necessarily been originated from that direction. Thus, each location of the sky contains photons coming from different regions of the last scattering surface. Producing a damping of the fluctuations. The scales affected by this smearing are those smaller than the horizon size at the redshift z_r of the rescattering epoch. On the other hand, the fraction of photons that are never rescattered is $e^{-\tau}$, where $\tau \equiv \sigma_T \int dt n_e$ is the optical depth, n_e is the electron density and σ_T is the Thomson cross-section.
- *Sunyaev-Zel'dovich effect (SZ)*: this effect induces a characteristic spectral distortion in the CMB and is produced by inverse Compton scattering of CMB photons during their passage through hot ionized gas, mainly in the inner regions of clusters of galaxies [136]. Let us assume that clusters are virialized objects, meaning that their kinetic energy is equal to minus one-half of their potential energy. They have very deep gravitational wells, and therefore, large kinetic energies that keep most of the intracluster hydrogen gas ionized. If a sufficient number of CMB photons traveling through the cluster are scattered to higher energies, this produces a noticeable change in the CMB spectrum of the order of 1 mK for hot massive clusters. High frequency photons will be blueshifted, whereas low frequency photons will be redshifted, with a changeover frequency around 217 GHz, see figure 1.5. This effect is known as the “thermal” SZ effect. There is another effect, known as “kinematic SZ effect” produced by the relative motion of the cluster with respect to the CMB. This effect is one or two orders of magnitude weaker than the thermal SZ effect and it is very difficult to detect.

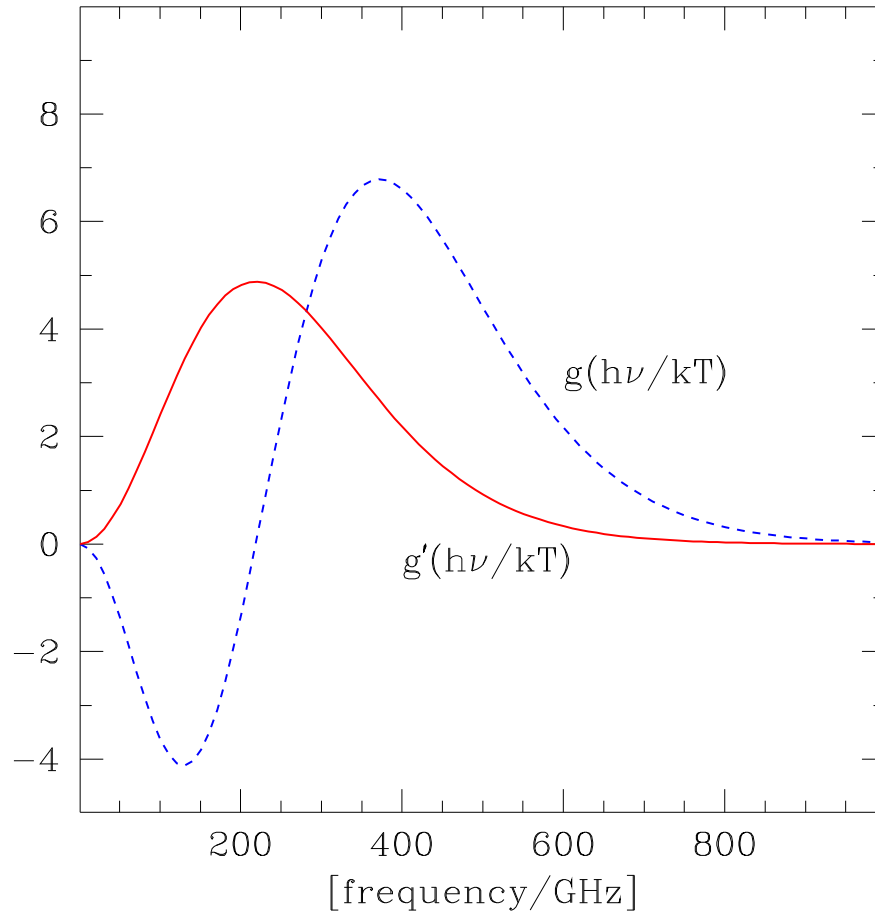


Figure 1.5 In this figure we show the frequency dependence of the intensity for the thermal Sunyaev-Zel'dovich effect (dashed-line) and the kinetic Sunyaev-Zel'dovich effect (solid line).

1.1.4 Foregrounds Contamination

When we observe the sky at microwave frequencies with state-of-the-art instrumentation we are not only collecting photons coming from the CMB. Actually these are just a fraction of all the photons that we see because there are several sources of contamination at microwave frequencies and it is the work of CMB scientists to study with a great deal of detail these contaminants in order to remove them properly. Most of this contamination is in the form of diffuse emission coming from our own Galaxy, although there is a significant contribution from extragalactic compact sources, such as galaxies and clusters of galaxies (Sunyaev-Zel'dovich effect). The purpose of this thesis is to study mechanisms for the detection of compact sources. The spectral behaviour of most of these components is approximately known. Some of them are brighter at lower frequencies, i.e. synchrotron and free-free emission, and some at higher frequencies, i.e. dust. As seen on figure (1.6) there is window at ~ 100 GHz where the Galactic contaminants have a minimum in their brightness and therefore, all the space-borne CMB experiments have detectors at these frequencies. But as we mentioned above, in order to obtain a clean signal from the CMB we need to study the frequency dependence of the contaminants at different frequencies. And this is the purpose of having several detectors at all the possible frequencies.

Moreover, not all the contaminants are from outer space. If our instrument is on the surface of the Earth or balloon-borne there is an important contamination coming from the Earth atmosphere that must be taken into account. Not to mention the possible interferences from ground and satellite communications in the microwave frequencies. Finally the instruments themselves introduce some instrumental noise and possible systematic effects that must be studied and understood in order to make a proper use of the data. Now let us review the characteristics of the main sources of contamination.

1.1.5 Galactic Components

Synchrotron

The synchrotron emission is the radiation produced by particles when they get accelerated by a magnetic field. Whereas for non-relativistic velocities (cyclotron radiation) the frequency of emission is simply the frequency of gyration in the magnetic field, for extreme relativistic particles the frequency spectrum is more complex and can extend beyond this gyration frequency. For a detailed description of this emission see Rybicki & Lightman [120] and Smoot [131]. The cyclotron frequency ω_B is

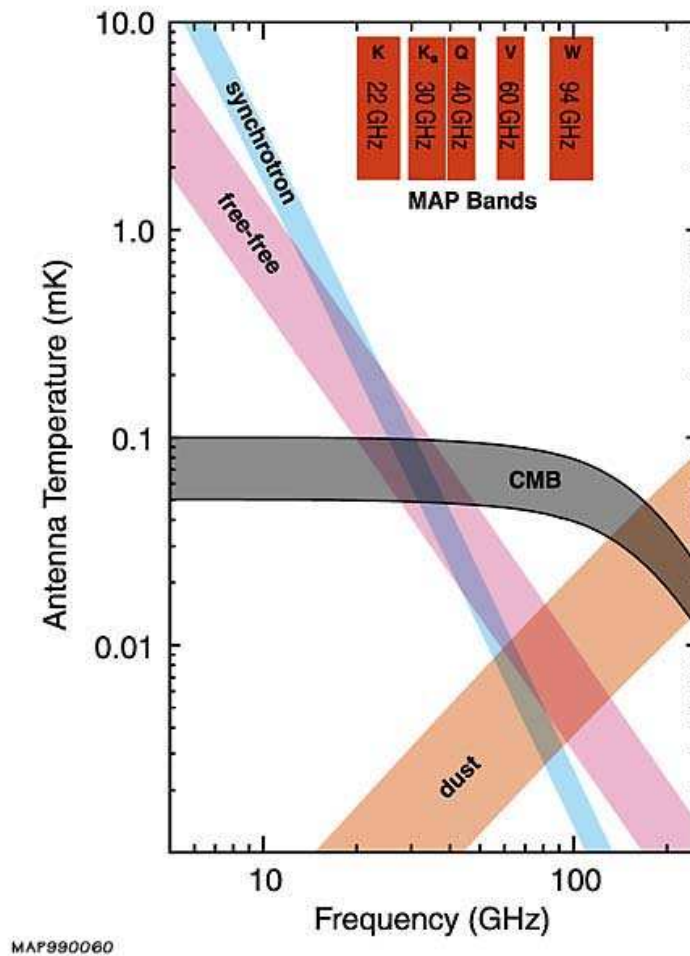


Figure 1.6 In this figure we can see the frequency dependence of the main Galactic contaminants of the CMB, synchrotron, free-free and dust emission. For the lower frequencies, the dominant emissions are free-free and synchrotron, whereas for higher frequencies the main source of contamination is dust. In between, at $\sim 60\text{-}90$ GHz, there is a *window* where the CMB dominates over the contaminants. Also shown are the 5 WMAP frequency bands between 23 and 94 GHz.

$$\omega_B = \frac{qB}{\gamma mc} \quad (1.1.10)$$

where q and m are the particle's charge and mass, respectively, B is the intensity of the magnetic field, c is the light speed and γ is the relativistic factor. Since each charged particle emits at the same gyration frequency, the spectrum of the cyclotron radiation is very simple. In the relativistic case the emission is beamed into a narrow cone of width $\Delta\theta = 2/\gamma$ and the frequency spectrum is more complex. Due to the beaming effect, an observer will see a pulse of radiation confined to a time period much shorter than the gyration period, i.e. γ^3 times shorter. Therefore, the spectrum will spread over a broader region with a cut off at the "critical frequency"

$$\omega_c = \frac{3}{2}\gamma^2\omega_B \sin\alpha = \frac{3\gamma^3 qB}{2mc} \sin\alpha \quad (1.1.11)$$

where $\sin\alpha$ represents the projection of the electron trajectory into a plane perpendicular to B . Then, if γ increases, the pulses are shorter and more harmonics of the fundamental ω_B contribute. In the case $\gamma \rightarrow \infty$, a large number of harmonics are needed to describe the emission and the envelope of this emission approaches the form of a certain function $F(x)$. The power per unit frequency emitted by each electron is:

$$P(\omega) = \frac{\sqrt{3}}{2\pi} \frac{q^3 B \sin\alpha}{mc^2} F\left(\frac{\omega}{\omega_c}\right) \quad (1.1.12)$$

where the function $F(x) \equiv x \int_x^\infty K_{5/3}(y) dy$, and $K_{5/3}$ is the modified Bessel function of 5/3 order.

The situation in our Galaxy is even more complicated, since particles with different velocities are present, and the magnetic field can vary from a point to another. It can be shown that, if we assume that the direction of motion of the electrons is random with respect to the magnetic field and that a power law can describe the electrons energy spectrum, then the synchrotron luminosity is given by:

$$I(\nu) = \frac{\sqrt{3}}{8\pi mc^2} q^3 \left(\frac{3q}{4\pi m^3 c^5}\right)^{(p-1)/2} L N_0 B_{eff}^{(p+1)/2} \nu^{-(p-1)/2} a(p) \quad (1.1.13)$$

where L is the length along the line of sight through the considered emitting volume, B_{eff} is the effective magnetic field strength along the line of sight and $a(p)$ is a weak function of the electron energy spectrum and is given by:

$$a(p) = \Gamma\left(\frac{p}{4} + \frac{19}{12}\right) \Gamma\left(\frac{p}{4} + \frac{1}{12}\right) \frac{1}{p+1} \quad (1.1.14)$$

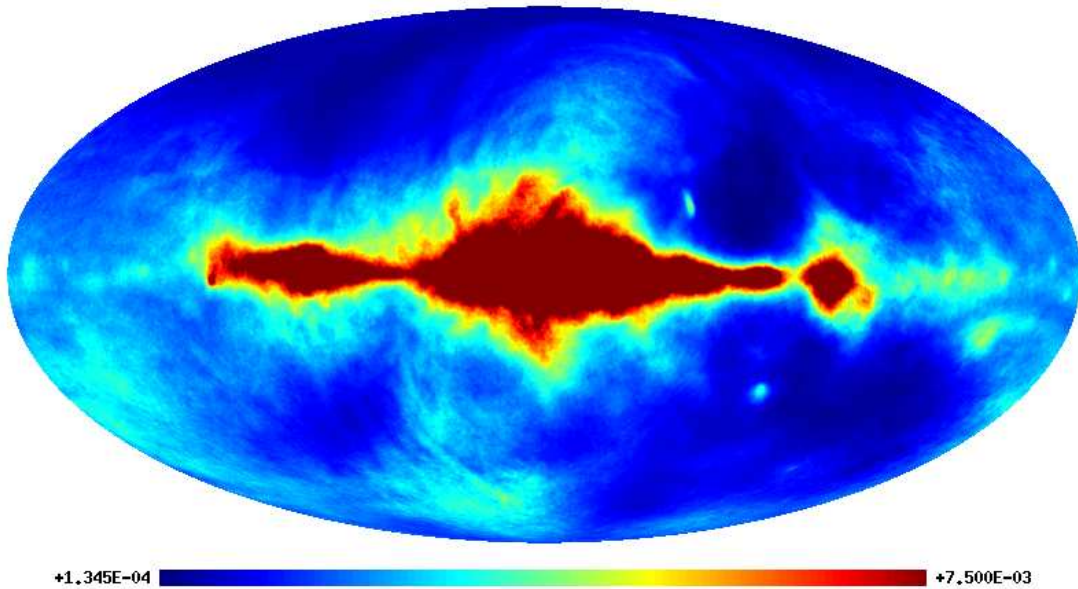


Figure 1.7 Synchrotron emission from the Planck Reference sky model. This is a cleaned version of the 408 GHz Haslam et al. [65] map made by Giardino et al. [49]. The map is in units of MJy/sr.

where Γ is the Gamma function. If we translate this luminosity in terms of brightness temperature, we obtain that

$$T(\nu) \propto \nu^{-(p+3)/2} = \nu^{-\beta}. \quad (1.1.15)$$

In our case, relativistic electrons are being accelerated by the magnetic field of the interstellar medium. Normally, these magnetic fields are very weak and do not produce significant synchrotron radiation to be detected. Most of the detected synchrotron emission comes from supernovae or active galactic nuclei and for frequencies below $\nu \sim 20$ GHz this is the dominant galactic emission. In fact, most of the surveys have been done in the MHz-GHz band. Before WMAP was launched, there existed only one all-sky synchrotron survey at 408 MHz [65] that has been widely used. In figure (1.7) we show a cleaned version of the Haslam 408 MHz, a synchrotron template used in the “Planck Reference Sky”¹, a compilation made within the Planck Collaboration with the latest templates for the different diffuse Galactic components, CMB, SZ clusters and point sources. There are several other surveys covering small fractions of the sky (see Smoot [131]), with the exception of the northern hemisphere survey at 1420 MHz [116] and the southern hemisphere at 2326 MHz [80].

¹<http://www.planck.fr/heading79.html>

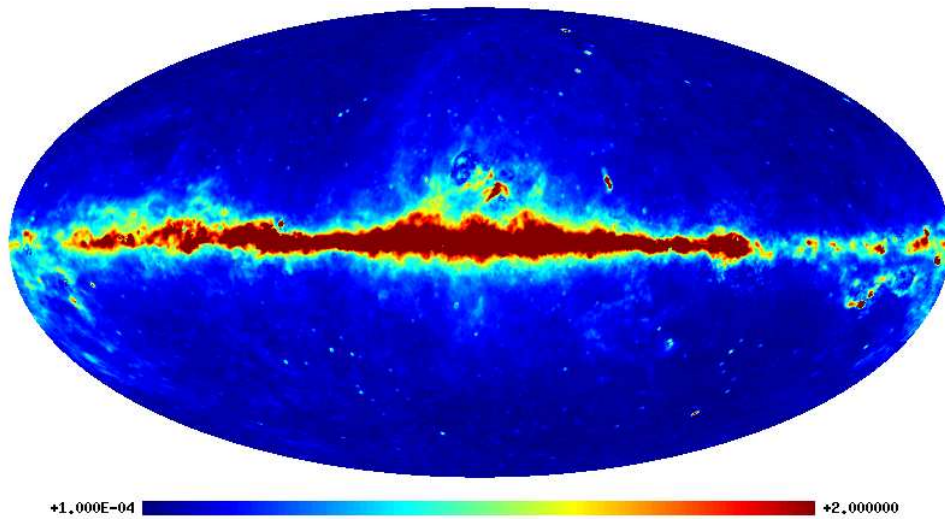


Figure 1.8 WMAP third year derived synchrotron template. It has been obtained using a MEM-based approach, using as a prior the Haslam et al. [65] map. The map is in units of mK. The procedure for creating the template is described in Hinshaw et al. [73].

In 2006 the WMAP team have published the results of three years of data and their subsequent analysis, including a new synchrotron template obtained using the WMAP K- and Ka-band data, at 23 and 33 GHz, respectively. This new template improves the widely used Haslam map at 408 MHz because, first, the intrinsic systematic measurement errors are smaller and, second, the low frequency Haslam map is less reliable at tracing microwave synchrotron emission because the synchrotron spectrum is non-uniform and this produces morphological changes in the brightness as function of frequency [11]. The WMAP team have used a Maximum Entropy Method approach (MEM) to obtain the best fit synchrotron emission map. As a prior of the synchrotron map needed by the method they used a modified Haslam map. The result from the MEM-based approach is shown in figure 1.8.

Free-Free

The Bremsstrahlung or free-free emission is an electromagnetic radiation produced when a charged particle is accelerated in the Coulomb field of another charged particle. In our case, these particles are free high energetic electrons ($T \sim 10^4$ K) interacting with ions of the interstellar medium. It has been named free-free because in this process the un-bound electrons remain un-bound after the interaction, as opposed to being captured into a bound state (free-bound) or making a transition between two bound states (bound-bound emission). This radiation is poorly known, it is difficult to measure and

dominates in a small range of frequencies ~ 50 GHz where the other Galactic contaminants, thermal dust and synchrotron, are minimum. The physics of the free-free radiation can be treated in a classical way because the derived expressions, for some regimes, have the correct functional dependences for most of the physical parameters. But since the photons produced in this kind of interactions can be very energetic, a quantum correction to the classical expressions may be obtained. A more detailed discussion about this radiation can be found in Dickinson, Davies, & Davis [38], Rybicki & Lightman [120], Smoot [130].

The expression for the total free-free emission per unit time, per unit volume and per unit frequency by a single electron is given by:

$$\frac{dW}{d\omega dV dt} = \frac{16\pi q^6}{3\sqrt{3}c^3 m^2 v} n_e n_i Z^2 g_{ff}(v, \omega) \quad (1.1.16)$$

where n_i and n_e are the ion and electron densities, q and m are the electron charge and mass, v is the velocity respect to the ion, c is the speed of light and Z is the ion's atomic number. The quantum Gaunt factor $g_{ff}(v, \omega)$ is the quantum correction and depends on the energy of the electron and on the frequency of the emission.

In our Galaxy there is a population of electrons with a certain velocity dispersion. If we extend the previous result to obtain the free-free emission of this population, it can be shown [120] that the total intensity – integrated along the line of sight – is given by

$$I(\nu) \propto T_e^{-0.5} e^{-\frac{h\nu}{kT_e}} \bar{g}_{ff} EM \quad (1.1.17)$$

where \bar{g}_{ff} is an average Gaunt factor and EM is the emission measure defined by:

$$EM = \int n_e n_i dl \quad (1.1.18)$$

being the integral along the line of sight. An approximation for \bar{g}_{ff} is given by Smoot [130].

$$\bar{g}_{ff} = 4.69 \left[1 + 0.176 \ln \left(\frac{T_e}{10^4 K} \right) - 0.118 \ln \left(\frac{\nu}{10 \text{ GHz}} \right) \right] \quad (1.1.19)$$

As we mentioned above, the free-free is a diffuse emission very difficult to measure. It is known that this radiation is correlated with other physical processes, i.e. H_α emission at 4.57×10^{14} Hz, and can be used as a tracer of the free-free radiation (although it requires to be corrected for dust absorption). Different authors derive slightly different expressions for the H_α , e.g. the expression derived by Smoot [130] is:

$$I_{H_\alpha} = 0.36 \left(\frac{T_e}{10^{-4}} \right)^{-0.9} EM[R] \quad (1.1.20)$$

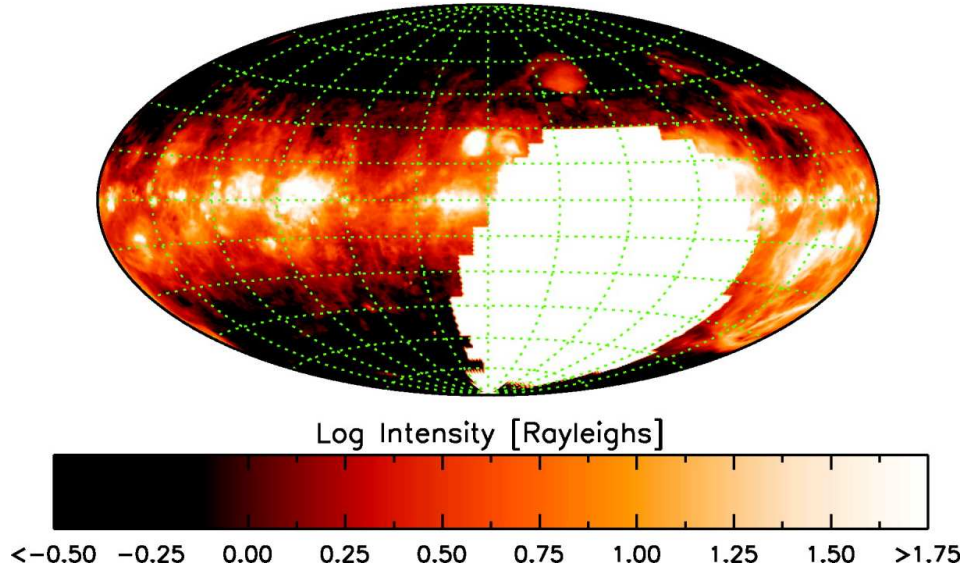


Figure 1.9 This image shows the total H_α intensity map and it was obtained by the Wisconsin H-Alpha Mapper (WHAM), an instrument designed to produce a survey of H_α emission from the interstellar medium over the entire northern sky, see <http://www.astro.wisc.edu/wham> for further information.

where 1 Rayleigh [R] is $2.41 \times 10^{-7} [\text{erg cm}^{-2} \text{s}^{-1} \text{sr}^{-1}]$. From the previous expression it can be derived that

$$I_{ff} \propto I_{H_\alpha} T_e^{0.4} e^{-\frac{h\nu}{kT_e}} \bar{g}_{ff} \quad (1.1.21)$$

In the last decade several H_α surveys have been conducted, such as the WHAM [61], VTSS [34], SHASSA [48] and the AAO/Schmidt survey. The most sensitive is WHAM (Wisconsin H Alpha Mapper), a survey in the northern hemisphere with 1 degree resolution covering $\delta \geq -30^\circ$ (see figure 1.9). The other relevant survey is SHASSA (Southern H Alpha Sky Survey Atlas), a survey in the southern hemisphere covering $\delta \leq +15^\circ$ (see figure 1.10).

As mentioned above, the WMAP have used three years of data to obtain new templates for the galactic foregrounds, in particular for the free-free emission. They have used a component separation method based on MEM, using as a prior of the free-free emission the full-sky H_α map compiled by Finkbeiner, Davis, & Schlegel [44] corrected for dust extinction [11], see figure 1.11. The resulting template for the free-free can be seen in figure 1.12.

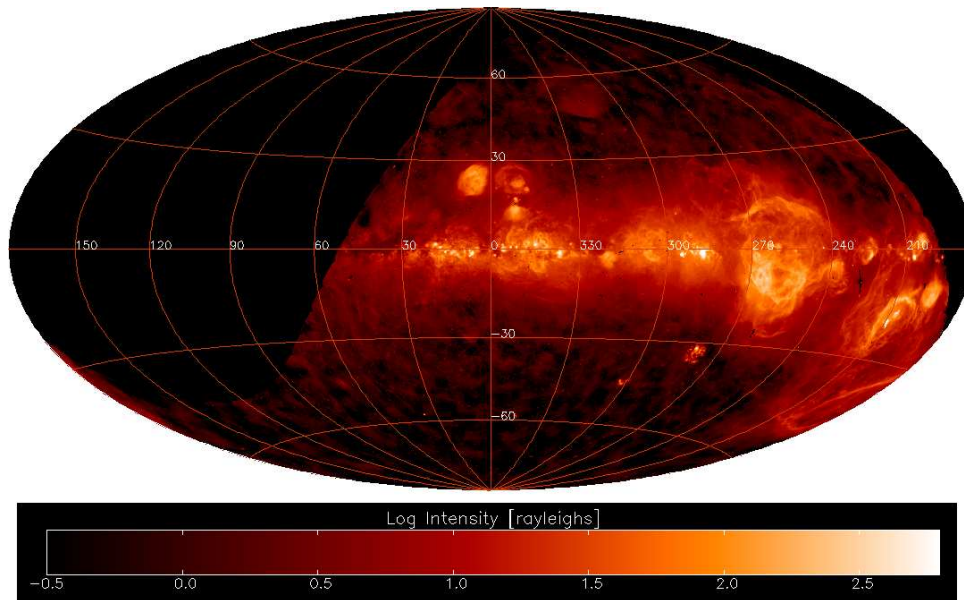


Figure 1.10 H_α Emission from the interstellar medium in the southern hemisphere obtained with the Southern H_α Survey Atlas (SHASSA), see <http://amundsen.swarthmore.edu/SHASSA> for further information.

Full-sky dust corrected Halpha map

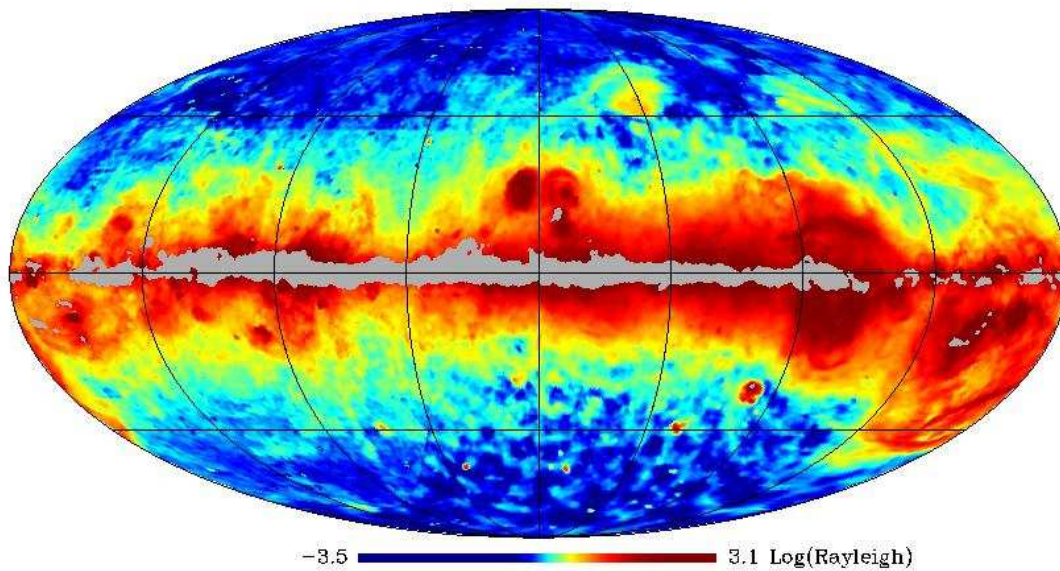


Figure 1.11 Full sky H_α map corrected for dust using the 100μ maps from Schlegel, Finkbeiner, & Davis [125]

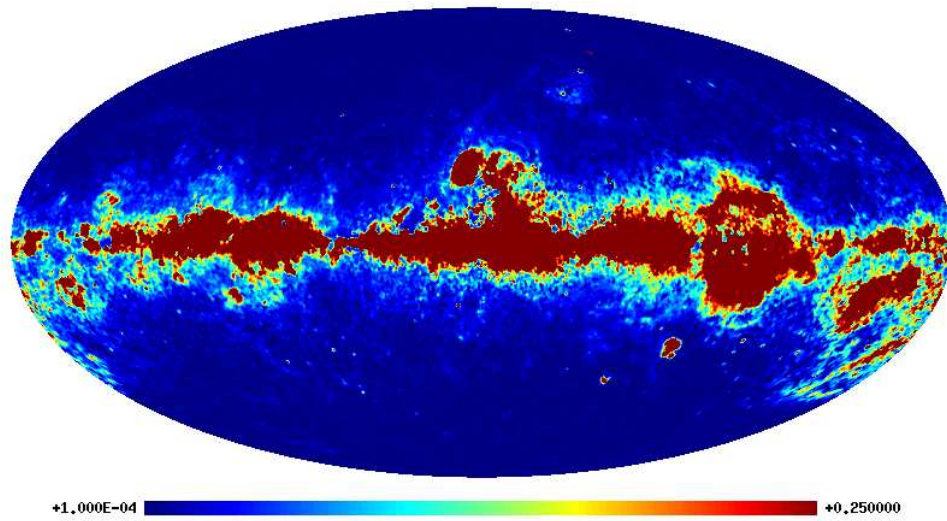


Figure 1.12 WMAP third year derived free-free template. It has been obtained from the difference of the WMAP K and Ka using a MEM-based approach. This map is in units of mK. The procedure for creating the template is described in detail in Hinshaw et al. [73].

Thermal Dust

The radiation that dominates the Galactic emission above 90 GHz is the emission produced by small grains of dust, just a few μm in size, that absorb the UV light from the interstellar medium re-emitting it in the far-infrared part of the spectrum. The thermal dust emission can be modeled by a modified black-body radiation, the so-called grey-body:

$$I_\nu \propto B_\nu(T_D)\nu^\alpha \quad (1.1.22)$$

where $B_\nu(T)$ is the black-body function, T_D is the dust temperature ($\sim 18\text{K}$) and ν^α represents the emissivity. Depending on the nature of the dust grains, the emissivity index varies [2]. A detailed study of the dust grain properties can be found in Desert, Boulanger, & Puget [35]. Several experiments have provided a significant amount of information about the dust emission, in particular IRAS (Infrared Astronomical satellite), COBE-DIRBE (Diffuse Infrared Background Experiment) and COBE-FIRAS (Far-infrared absolute spectrophotometer). Using this information [125] have produced a thermal dust emission map at $100\mu\text{m}$. This model reproduces the emission at $\nu \in [1250, 3000]$ GHz, with an emissivity $\alpha = 2$ with dust temperature varying between 17 and 21 K. The resultant template has an angular resolution of 6° . Finkbeiner, Davis, & Schlegel [44] obtained a multi-component model capable of describing the dust emission from $\nu = [100, 3000]$ GHz. This model is a combination of two grey bodies with

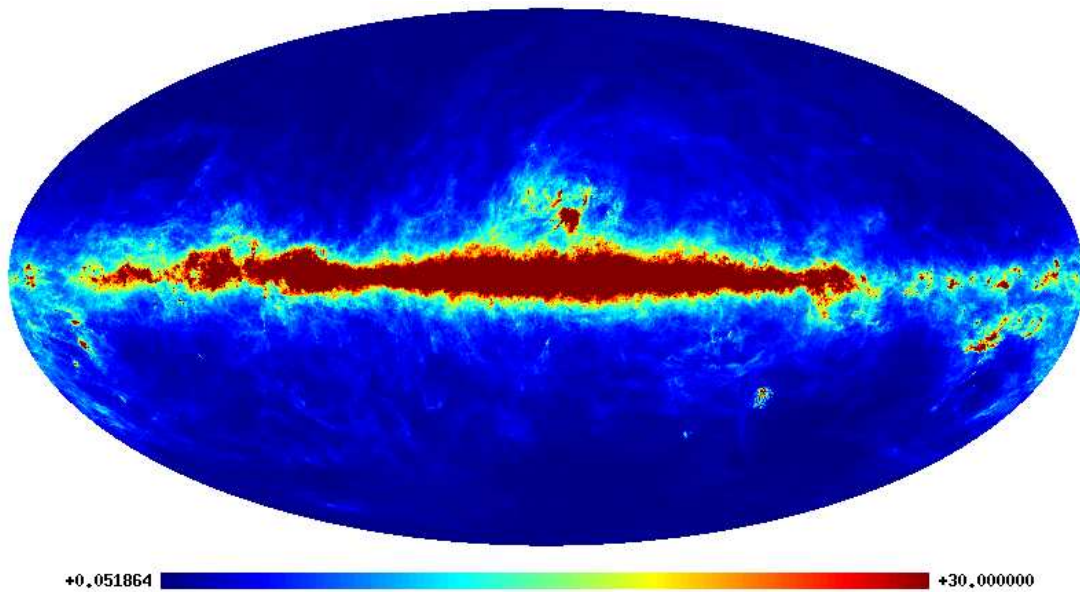


Figure 1.13 Thermal dust emission map at 857 GHz obtained from a combination of two grey-bodies with mean emissivity $\alpha_1 = 1.67$ and $\alpha_2 = 2.70$ and mean temperatures $T_1 = 9.4$ K and $T_2 = 16.2$ K. The map is in units of MJy/sr.

mean emissivity parameters $\alpha_1 = 1.67$ and $\alpha_2 = 2.70$ and mean temperatures $T_1 = 9.4$ K and $T_2 = 16.2$ K. The resulting template for the dust component is shown in figure 1.13

In the last years an anomalous Galactic emission at low frequencies has been possibly detected that can not be accounted as thermal dust or free-free emission. Moreover, several authors have shown a correlation with thermal dust [83, 85, 106, 151]. A new process that could explain this anomalous radiation was proposed by Draine & Lazarian [40, 41]. This process has a frequency dependence similar to that of the free-free emission in a certain range of frequencies, but with a larger intensity, and is produced by rotational electric dipole emission and, thus, has been named “spinning dust”.

A careful study of the spinning dust can be found in Draine & Lazarian [40, 41]. In the last years an increasing number of groups have reported on possible detections of spinning dust, although none of them seems to be definitive. The WMAP group have analyzed their three year data searching for evidences of this emission but no significant result has been reported. They conclude that higher quality diffuse measurements of the microwave sky at 5-15 GHz will be necessary to further understand this process. A detailed compilation of the experiments that have reported on this anomalous emission can be found in Hinshaw et al. [73].

1.1.6 Extragalactic Components

Point Sources

The contamination of the CMB due to the extragalactic point sources is an important problem and must be studied in detail. As compared with other contaminants, the frequency dependence of extragalactic point sources is not very well known in the GHz range. An important effort has been made in the last decade to model the different population of sources. These populations can be divided into two differentiated groups, radio sources and infra-red/sub-millimeter (IR/sub-mm) sources. Radio emitting extragalactic sources in the GHz range are mainly active galactic nuclei (AGN), with a strong non-thermal emission originated in the center of the Galaxy. This emission is synchrotron radiation produced by relativistic electrons moving along magnetic fields. The IR/sub-mm emission is produced by the dust, that absorbs UV and optical radiation re-emitting it in the far-infrared part of the spectrum. This part of the point source spectrum is poorly known, although in the last several years new surveys in this frequency range have been conducted and more detailed theoretical models have been proposed.

The models that describe the populations of radio and IR/sub-mm galaxies use the so-called “source number counts” (number of sources per stereoradian and per flux interval) that take into account the number of objects from a certain population and their corresponding flux. The differential number counts per stereoradian dN/dS in a given flux interval are:

$$\frac{dN}{dS} = \int_{z_i}^{z_h} dz \frac{dV}{dz} \frac{dL(S; z)}{dS} \psi[L(S; z), z], \quad (1.1.23)$$

where $\psi[L(S; z), z]$ is the redshift dependent luminosity function and dV/dz is the volume element per unit solid angle. Moreover, the integral number counts describe the number of source per stereoradian with a flux above a given minimum flux, S_{min} :

$$N(> S_{min}) = \int_{S_{min}}^{S_{lim}} \frac{dN}{dS} dS, \quad (1.1.24)$$

where S_{lim} is the flux limit for detecting sources. The flux S is related to the intrinsic luminosity within a given frequency interval as follows:

$$S_{\Delta\nu} = \frac{L_{\Delta\nu} K(L, z)}{4\pi d_L^2} \quad (1.1.25)$$

where d_L is the luminosity distance and $K(L, z)$ is the K correction. For a more detailed review of this topic see De Zotti et al. [30].

Regarding the radio sources, number counts have been obtained from VLA observations for very low flux limits, $\sim \mu\text{Jy}$, at 1.41, 4.86 and 8.44 GHz [103] and the models behave very well at this frequency range. For higher frequencies, where there is a lack of observations, there has been an increasing effort in modeling the spectral properties and evolution of the source populations.

In the last decade, several groups have studied the observations of radio sources at frequencies below 8 GHz [42, 79, 141] and proposed models that explain the observations. In particular, the model by Toffolatti et al. [141] has been widely used in the last years. This model fits well the source number counts for $\nu \leq 30$ GHz with a flux limit of ~ 20 mJy.

In the last year, a new model for the radio source has been proposed by De Zotti et al. [32], improving the existing model by Toffolatti et al. [141]. In this work, they study the contributions to the counts by different source populations in the range of 20 – 30 GHz. They have produced new evolutionary models for the flat-spectrum radio quasars, BL Lac objects and steep-spectrum sources based on the latest observations, see De Zotti et al. [32] for further details on the surveys. They also take into account the synchrotron and free-free emission when estimating the counts of different populations of star-forming galaxies. In figure 1.14 we show a comparison of the Toffolatti et al. [141] model with the De Zotti et al. [32] model.

Following the latest model by de Zotti et al., figure 1.16 shows a full-sky simulation of point sources at 30 GHz.

Regarding the IR/sub-mm galaxies, the models available just a few years ago did not match the latest observations with SCUBA and MAMBO. Then a new population of proto-spheroidal galaxies was introduced by Granato et al. [53, 54], see these works for further details. To summarize, the latest model by De Zotti et al. [32] is the one that better describes the radio galaxies number counts below $\nu \leq 150$ GHz, whereas for frequencies well above $\nu \geq 150$, where dusty spheroids dominate, the best model available today is the Granato et al. [53, 54] model.

In 2003, NASA's WMAP satellite team published the results of the analysis of the first year of available data. The five instruments on-board this satellite cover the range 23 – 94 GHz, and the study of the brightest point sources at these five frequencies yielded a catalog with 208 sources [11]. In 2006, with three years of data, they have published a new catalog with 323 objects, giving for most of them an estimation of the flux density at each of the frequencies [73]. In López-Caniego et al. [91], we have used a non-blind approach to study a few thousands of objects observed at 5GHz in the WMAP three-year data. As a result, we have provided a catalogue with 938 objects

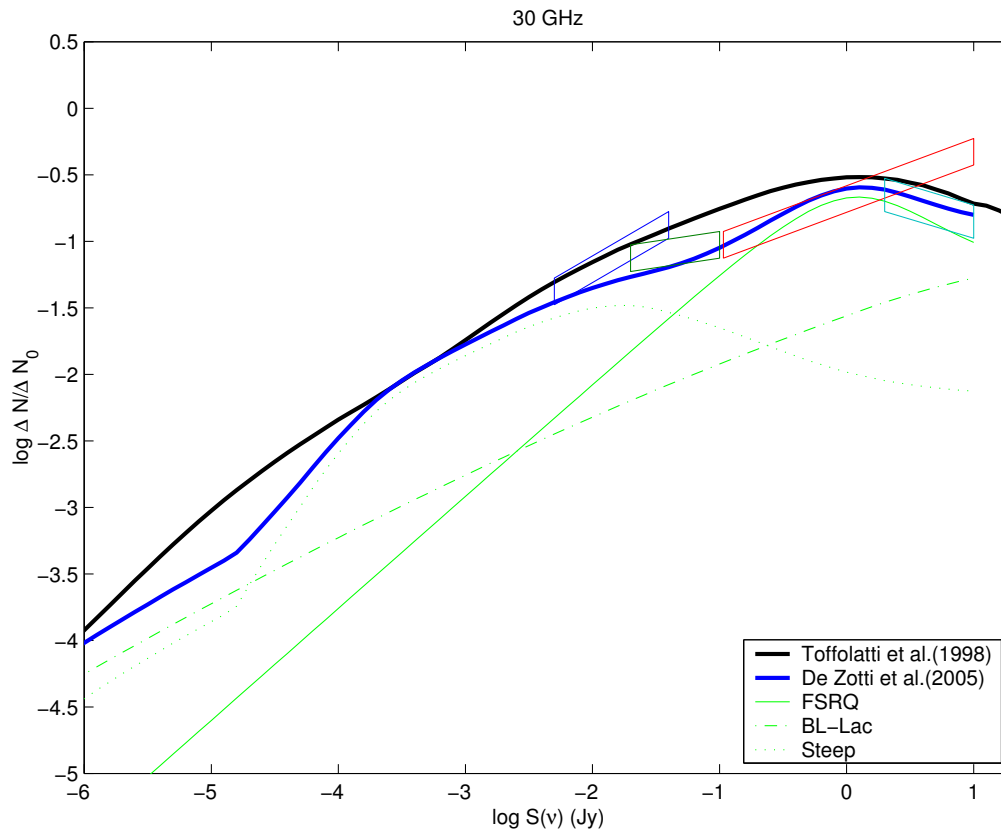


Figure 1.14 Source number counts predicted by the Toffolatti et al. [141] model (black solid line) and the new De Zotti et al. [32] (blue solid line) at 33 GHz (normalized to the expected number counts for an Euclidean universe). For the latter model, the number counts for three sub-populations of radio-sources are also shown, flat-spectrum sources (solid green line), BL-Lac (green dashed line) and steep-spectrum sources (green dotted line). The 1σ boxes correspond to observational results CBI (31 GHz, blue), VSA (33 GHz, green), DASI (31 GHz, red) and WMAP 1st year (33 GHz, cyan).

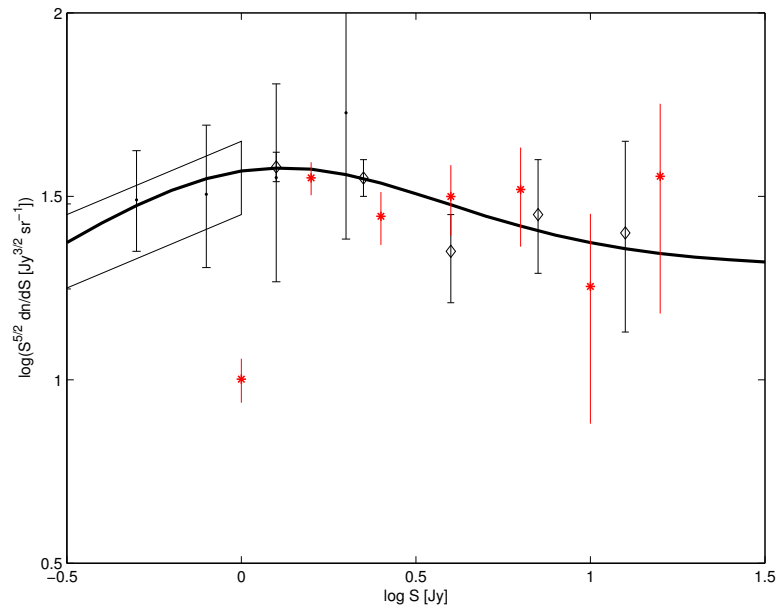


Figure 1.15 Number counts multiplied by $S^{5/2}$. *Red asterisks*: counts from the $NEWPS_{5\sigma}$ catalogue at 33 GHz from López-Caniego et al. [91]. *Black diamonds*: WMAP counts [73]. *Black dots*: ATCA 18 GHz pilot survey counts [119]. The parallelogram is from the DASI experiment at 31 GHz [82]. The solid curve shows, for comparison, the counts predicted by the model by De Zotti et al. [32].

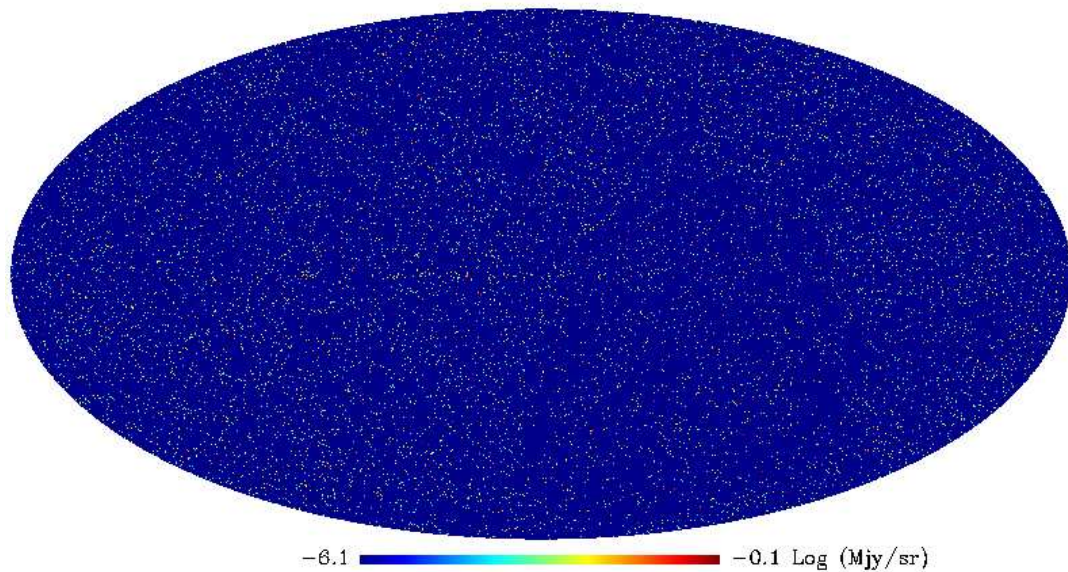


Figure 1.16 Full-sky simulation of point sources at 30 GHz (in Log scale) following the latest source number counts models by De Zotti et al. [32], made by J.González-Nuevo. The map is in units of Mjy/sr.

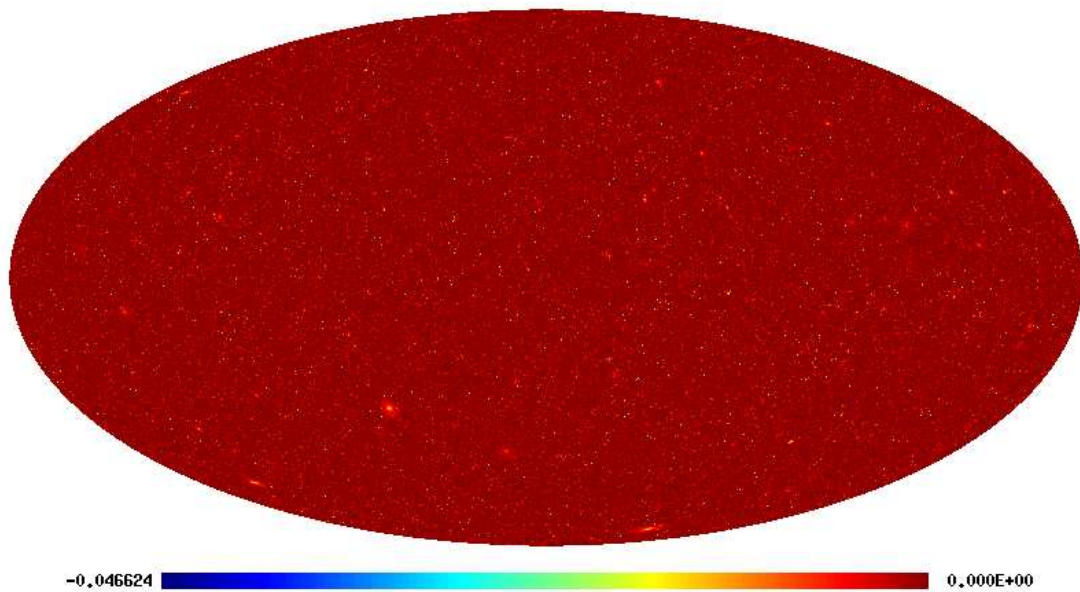


Figure 1.17 SZ clusters simulations for the *Planck Reference Sky* at 70 GHz. The map is in units of MJy/sr.

with an estimation of their flux, error and spectral index at the five WMAP frequencies.

Sunyaev-Zel'dovich effect from clusters of galaxies

The Sunyaev-Zel'dovich effect is considered a secondary anisotropy of the CMB as it was described in section (1.1.3). This effect arises from the frequency shift when CMB photons are scattered by the hot electrons in the intra-cluster gas. It has a characteristic frequency dependence with a temperature decrement for frequencies below 217 GHz and a temperature excess at higher than 217 GHz as shown in figure 1.5. In figure 1.17 we show a full-sky simulation of SZ clusters made by P. Mazzotta used in the *Planck Reference Sky*.

1.2 The Component separation problem

In the previous section we have reviewed the origin of the CMB radiation. Then, we have summarized the different sources of contamination that must be considered when studying the CMB, in particular, the diffuse emissions from our Galaxy (dust, free-free and synchrotron radiation) and the most important to us, the compact source emission from extragalactic point sources and Sunyaev-Zel'dovich clusters. From a practical point of view, the process of observing the sky at microwave frequencies and separat-

ing the CMB signal from all the contaminants is not trivial. In the last decade there has been a significant effort developing techniques that can separate a certain component from the others. Depending on one's interest, the component to be separated could be the CMB radiation, the point sources or any of the diffuse galactic emissions. Moreover, the separation of one component or the other requires very specific procedures tailored for this purpose. The same procedure to separate the CMB from the synchrotron will not be the same as the one to obtain the compact sources. Some techniques approach this kind of analysis in a Bayesian way, taking into account *a priori* information about the components to be separated, and other techniques do it blindly. Some techniques work on a pixel-by-pixel basis, whereas other deal with maps. Some of the methods that have been proposed are Wiener Filtering (WF) [17, 138], Maximum Entropy Method (MEM) [6, 74, 75, 135], Fast Independent Component Analysis (FastICA) [93, 94], Spectral Matching Independent Component Analysis (SMICA) [29, 110] and Mexican Hat Wavelet (MHW) [19, 145].

1.2.1 Techniques for the extraction of point sources

Among the different methods that have been used in the component separation problem, *filtering* is specially well suited for the detection of compact sources embedded in a noisy background (e.g., the mixture of CMB and the Galactic contaminants).

In the context of compact source detection a filter is a *device* that transforms the data in such a way that, after filtering, we have increased the signal-to-noise ratio (SNR) of the objects we are trying to detect. From the mathematical point of view, a filter is an operator:

$$L : f(x) \rightarrow g(t) = L f(t) \quad (1.2.1)$$

where f is the input signal, g is the output signal and t is the independent variable. The filter is linear if the filtered quantity g is a linear functional of the inputs, and the filter is homogeneous if the output is delayed by τ when the input is delayed by τ , $g(t - \tau) = L(f(t - \tau))$. Most of the filters used in a wide range of disciplines are linear and homogeneous.

The homogeneity is a desirable property of a filter. If we let δ be the Dirac distribution, then if f is continuous, its value at t is obtained by the integral:

$$f(t) = \int_{-\infty}^{\infty} f(u)\delta(t - u)du. \quad (1.2.2)$$

The continuity and linearity of L imply that

$$Lf(t) = \int_{-\infty}^{\infty} f(u)L\delta(t-u)du. \quad (1.2.3)$$

Now let us define h as the impulse response of L , $h(t) = L\delta(t)$. Due to the homogeneity property of the operator, $L\delta(t-u) = h(t-u)$ and hence

$$Lf(t) = \int_{-\infty}^{\infty} f(u)h(t-u)du = \int_{-\infty}^{\infty} h(u)f(t-u)du = h \otimes f \quad (1.2.4)$$

where \otimes denotes convolution. Therefore, a homogeneous linear filter is equivalent to a convolution with the impulse response h . This property is very useful if we decide to work in Fourier space, because if we use the convolution theorem we obtain that

$$Lf(t) = g(t) = h \otimes f(t) = \int_{-\infty}^{\infty} \hat{h}(q)\hat{f}(q)e^{-iqt}dq, \quad (1.2.5)$$

where we have taken into account the following convention for the Fourier transform:

$$\hat{f}(q) = \frac{1}{2\pi} \int_{-\infty}^{\infty} f(t)e^{iqt}dt, \quad (1.2.6)$$

$$f(t) = \frac{1}{2\pi} \int_{-\infty}^{\infty} \hat{f}(q)e^{-iqt}dq, \quad (1.2.7)$$

where the Fourier transform \hat{h} of the impulse response h is known as the transfer function of the filter. These considerations are valid for continuous signals, although it can be generalized to discrete data.

From the previous expressions we see that filtering an image with a linear homogeneous filter is equivalent to multiply the Fourier transform of the data with a transfer function, which in Fourier domain can be considered as a *frequency-selective* device, frequency in the sense of Fourier mode. This will be of great interest to us, because using the appropriate transfer function we will be able to reduce the contribution of those frequencies corresponding to the noise. Moreover, since we know the frequency range where the contribution from compact objects is significant, we can design a transfer function that preserves these frequencies, while reducing the contribution of the background noise present in the data.

This is the idea behind the widely used band-pass filters, where the filter is set to zero outside the desired range of frequencies (see figure 1.18)

$$\hat{h}(q) = \begin{cases} 1, & \text{if } |q| < q_c \\ 0, & \text{if } |q| \geq q_c \end{cases} \quad (1.2.8)$$

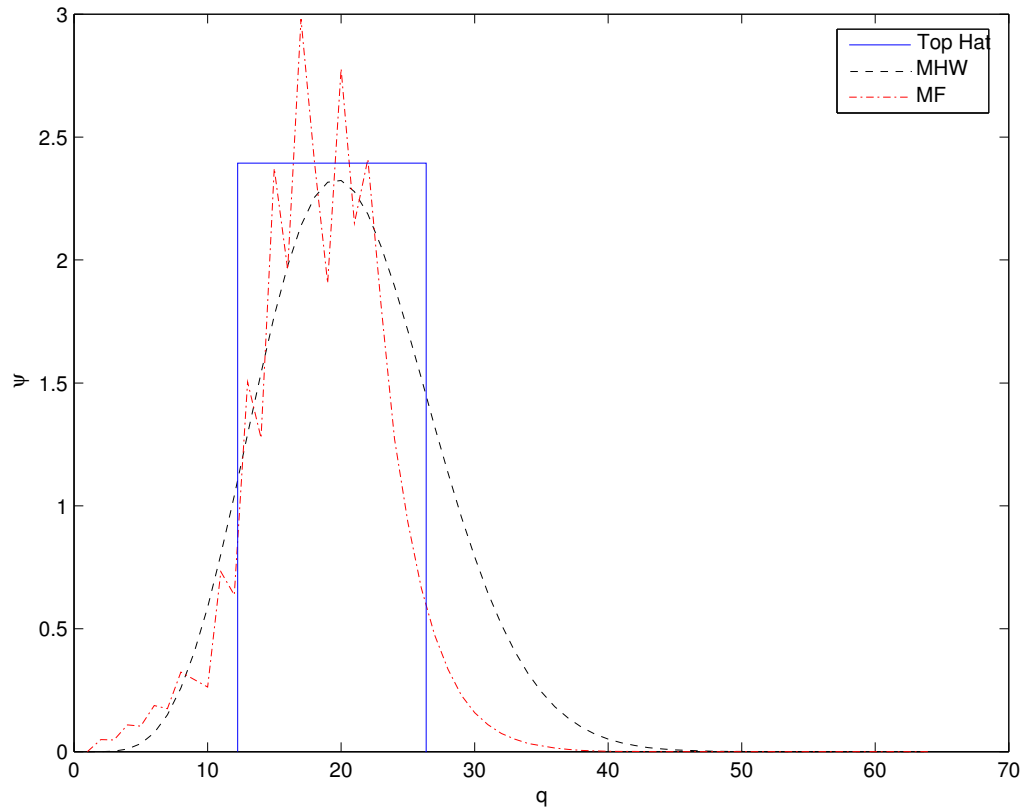


Figure 1.18 In this figure we show three commonly used filters in the literature. The solid blue line corresponds to the top-hat filter, the black dashed line to the Mexican Hat wavelet and the dot-dashed red line to the Matched filter for a typical CMB image. Note that they are plotted in Fourier domain.

where q_c is the cutoff frequency. The region $|q| < q_c$ is the pass-band of the filter, whereas the region $|q| \geq q_c$ is called stop band.

The impulse response of this filter is

$$h(t) = 2q_c \frac{\sin(q_c t)}{t} \quad (1.2.9)$$

and this kind of attenuated oscillations will introduce ring-shaped artifacts in the image in real space. These effects are due to the discontinuous shape of the transfer function and, even though this kind of filter has been extensively used in many areas of signal processing, we will not use it for the detection of compact sources in astronomical images.

It is desirable to have a continuous filter in Fourier domain, we would like to design a filter that transforms the data, a mixture of *signal + noise*, in such a way that after the filtering process we recover a *signal + a reduced noise*. This is what we call “optimal filtering”, a definition that needs further explanation, because one filter can be optimal for one purpose and totally inappropriate for another. In the following section we will review some of the common filters used to detect point sources. In the following chapters we will then review the new filters that we have developed, in particular, the “Modified Matched Filter” [86], the “Biparametric Scale-Adaptive Filter” [87, 88] and the various members of the “Mexican Hat Family of Wavelets” [51, 90]. See Herranz [67] and Barreiro [7] for detailed review of filters used for the detection of compact sources.

The Matched or Adaptive Filter

Let us consider a signal s with amplitude A at the position x_0 embedded in a noisy background n with dispersion σ . The signal-to-noise ratio (SNR) is

$$s/n = \frac{s(x_0)}{\sigma} = \frac{A}{\sigma} \quad (1.2.10)$$

and our ability to detect the signal will be proportional to the SNR. Now, let us define the “gain” or “amplification” λ of a signal obtained with a given filter

$$\lambda = \frac{s_\psi(x_0)/\sigma_\psi}{s(x_0)/\sigma} \quad (1.2.11)$$

where $s_\psi(x_0)$ is the filtered map at the position of the source and σ_ψ is the dispersion of the filtered map. If the amplification is greater than one, the signal-to-noise contrast

has increased in the filtered map improving the chances of detection.

It is possible to maximize λ , the gain of the filter, making $s_\psi(x_0) = s(x_0)$ while minimizing σ_ψ . If we perform this minimization in Fourier space, it can be proven that the filter that satisfies this minimization is

$$\Psi(q) \propto \frac{s(q)}{P(q)} \quad (1.2.12)$$

where $s(q)$ is the Fourier transform of the signal profile $s(t)$ and $P(q)$ is the power spectrum of the data. Note that we have assumed that the noise can be reproduced by an homogeneous and isotropic random field characterized by the power spectrum $P(q)$, i.e., $\langle n(\vec{q})n^*(\vec{q}') \rangle = P(q)\delta^n(\vec{q} - \vec{q}')$, $q \equiv |\vec{q}|$.

where $n(\vec{q})$ is the two-dimensional Fourier transform of the noise.

As an example, let us derive the two-dimensional matched filter for a compact source $s(x) = A\tau(x)$ with spherical symmetry, where A is the amplitude and $\tau(x)$ is the profile of the source. First, we consider a two-dimensional vector $y(\vec{x}) = s(\vec{x}) + n(\vec{x})$, where $n(\vec{x})$ is the background noise. Then, for a given filter ψ with spherical symmetry, the filtered field w is given by

$$w(\vec{x}) = \int y(\vec{q})\psi(q)e^{-i\vec{q}\vec{x}}d\vec{q}. \quad (1.2.13)$$

Assuming that the source is at the origin, the filtered field at the position of the source is given by

$$w(\vec{0}) = 2\pi \int_0^\infty qs(q)\psi(q)dq, \quad (1.2.14)$$

and the variance of the filtered field is

$$\sigma_\psi^2 = 2\pi \int_0^\infty qP(q)\psi^2(q)dq. \quad (1.2.15)$$

where $P(q)$ is the power spectrum. We want to find the filter ψ that satisfies the following conditions:

- $\langle w(\vec{0}) \rangle = A$, the filter is an unbiased estimator of the source amplitude.
- the filtered field has minimum variance σ_ψ^2 .

The first condition yields the constraint $\int q\tau(q)\psi(q)dq = 1/(2\pi)$. Using this constraint with a Lagrange multiplier, and following condition two, we minimize the variance of

the filtered map

$$L(\psi) = \sigma_{\psi}^2(\psi) + \lambda \left[\int q\tau(q)\psi(q)dq - \frac{1}{2\pi} \right]. \quad (1.2.16)$$

Taking variations with respect to ψ and setting the result to zero, we find expression (1.2.12)

$$\psi(q) = C \frac{\tau(q)}{P(q)} \quad (1.2.17)$$

where C is the appropriate normalization

$$C = \left[2\pi \int q \frac{\tau^2(q)}{P(q)} dq \right]^{-1}. \quad (1.2.18)$$

For example, let us consider a compact object in the sky (a Dirac- δ signal) that is observed with an instrument with a Gaussian point spread function, where σ is the width of the profile. Regarding the noise, we know that the instrument adds a certain amount of white instrumental noise. Now, let us assume that the power spectrum of the image is dominated by the noise, the point-like object contribution is minimal, and, therefore, the $P(q)$ is approximately constant. Then, the matched filter obtained from this image would be proportional to a Gaussian of width σ . It is a very well known result that the Gaussian filter is optimal for denoising signals with Gaussian profiles embedded in white noise.

However, the previous example can be considered as *ideal* if we compare it with the images with which we deal in everyday life, where the matched filter has some very well known problems. In order to define the matched filter in an appropriate way, first, it is necessary to estimate the value of the power spectrum for all the Fourier modes present in the image, which is specially difficult for the low modes where the power spectrum is *noisy*. Second, the use of such a noisy power spectrum to construct the MF often yields a filter with many discontinuities in Fourier space which, in turn, produces ringing effects in the filtered image (see figure 1.19). Therefore, some smoothing in the spectra needs to be done before constructing the filter, which introduces further arbitrariness. Third, sometimes it will not be possible to properly estimate some Fourier modes, for example when using masks with missing data, and these modes will have to be guessed.

Wavelets as Filters: Mexican Hat Wavelet Family

Several techniques based on wavelets have been developed in the last decades for dealing with data compression, pattern recognition, denoising, etc. It is only in recent years that wavelets have been used to detect point sources in astronomical images. They have an interesting property that makes them very useful, they retain information about the

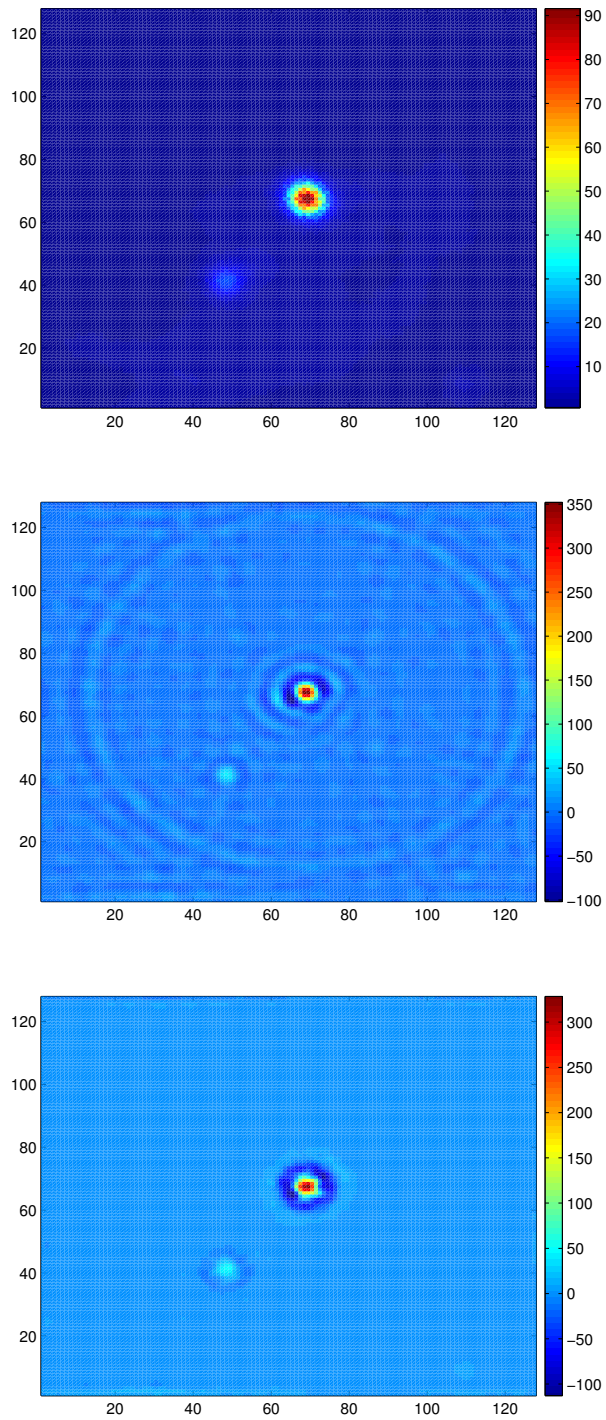


Figure 1.19 In the top panel we show the image before being filtered. In the middle panel we show the ringing effects produced by the Matched Filter when the power spectrum of the image is not well determined, as compared with the lower panel, where the image has been filtered with the MHW2 (the second member of the Mexican Hat Wavelet Family)

scale and position of the image. Unlike the Fourier transform, the wavelet transform allows one to have information about the importance of different scales at each position.

Let us consider the *discrete wavelet transform* (DWT). The wavelet basis is constructed from dilations and translations of the mother wavelet ψ (or analyzing wavelet) and the scaling function ϕ :

$$\psi_{j,l} = 2^{j/2}\psi(2^j t - l) \text{ and } \phi_{j,l} = 2^{j/2}\phi(2^j t - l), \quad (1.2.19)$$

where j and l are integer numbers denoting the dilation and translation indexes, respectively, and ψ and ϕ are chosen to be orthogonal and satisfy certain mathematical relations [27]. In particular, they must satisfy that:

$$\int \psi(t)dt = 0 \text{ and } \int \phi(t)dt = 1. \quad (1.2.20)$$

The reconstruction of the signal $f(t)$ using the wavelet basis is given by

$$f(t) = a_{0,0}\phi_{0,0}(t) + \sum_j \sum_l w_{j,l}\psi_{j,l}(t) \quad (1.2.21)$$

where a and w are the wavelet coefficients and are defined as

$$a_{0,0} = \int f(t)\phi_{0,0}(t)dt, \quad w_{j,l} = \int f(t)\psi_{j,l}(t)dt. \quad (1.2.22)$$

The expression (1.2.21) can be interpreted as the sum of a low resolution, smoothed function plus a series of consecutive refinements that carry information about the details of the function $f(t)$. The difference between the refinement level j and the next is giving us information about the structure of f at the scale j . Therefore, the scaling function ϕ carries information about structures of a certain scale inside a region. For this reason they are very useful for the point-source detection problem, because they can separate structures from a given scale, those with the same scale as that of the wavelet, while reducing the contribution of the other scales .

Now, let us consider the *continuous wavelet transform* (CWT). Instead of using an integer number of dilations and translations, we allow them to vary continuously. Then, for $R > 0$, where R is the scale of the wavelet, and $b \in \mathbb{R}$,

$$\psi_{R,b}(t) = R^{-1/2}\psi\left(\frac{t-b}{R}\right). \quad (1.2.23)$$

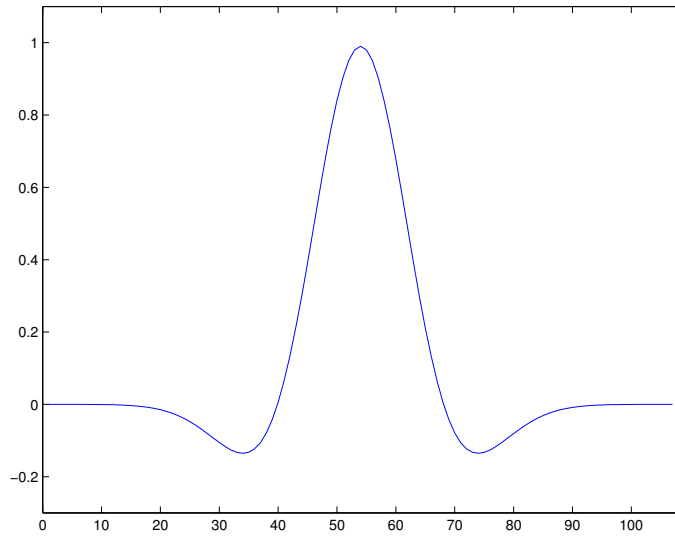


Figure 1.20 Normalized one-dimensional Mexican Hat wavelet in real space.

The continuous wavelet transform is thus defined as

$$Wf(R, b) = \int_{-\infty}^{\infty} f(t)\psi_{R,b}(t)dt = f \otimes \bar{\psi}_R(b), \quad (1.2.24)$$

where $\bar{\psi}_R(t) = R^{-1/2}\psi(-t/R)$. As an example, let us consider the well known “Mexican Hat wavelet”, a wavelet that has been extensively used in the literature for the detection of point sources with Gaussian profiles [19, 87, 144]. This wavelet is obtained applying the Laplacian operator to the Gaussian function of width R (see figure 1.20) and in two dimensions has the following expression

$$\psi(x) = \frac{1}{\sqrt{2\pi}} \left[2 - \left(\frac{x}{R} \right)^2 \right] e^{-\frac{x^2}{2R^2}}. \quad (1.2.25)$$

We remark that wavelets are compensated, i.e., the integral below the curve is zero and using them as filters helps to remove background contributions with scales of variation larger than the one of the wavelet. If we further apply the Laplacian operator to the Gaussian function we obtain a *family of wavelets*. The first members of this family have been studied [51] and it has been found that the first one, the previously mentioned *Mexican Hat Wavelet*, and the second, the *Mexican Hat Wavelet 2*, are the most suitable for the detection of point sources. In figure 1.21 we show the performance of the MHW when dealing with the detection of point sources. In the upper left panel we shown a simulation of Galactic diffuse emissions. In the upper right panel we show a simulation of point sources and instrumental noise. In the lower left panel we have added the previous two maps, and the result of filtering it with the MHW is shown in the lower

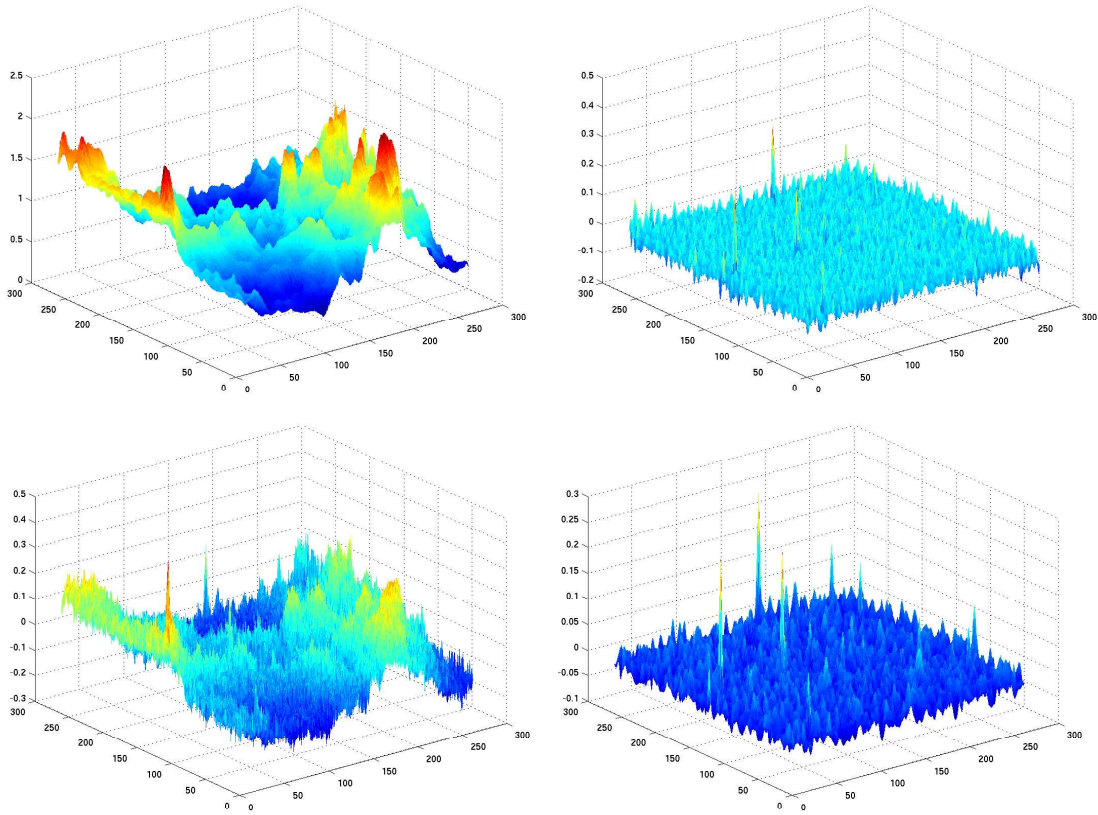


Figure 1.21 In this figure we show the performance of the Mexican Hat Wavelet. In the upper left panel we have a patch of the diffuse galactic contamination at 857 GHz, where dust is dominant. In the upper right panel we show a simulation of point sources + instrumental noise. In the lower left panel we have added the previous two components (dust, point sources and instrumental noise). Finally, when we filter the previous image with the Mexican hat wavelet at the optimal scale we obtain another image where most of the dust contribution and some of the noise has been removed.

right panel.

In the following chapters we will show practical applications of wavelets in the field of point source detections, from simple backgrounds, such as white noise, to the most realistic simulations of the *Planck Reference Sky*. In the last chapter, we will show the application of these techniques to real data from the WMAP third-year data. The main results of these analysis can be found in López-Caniego et al. [90, 91].

Bayesian approach

Most of the techniques developed for the detection of compact sources in CMB astronomy are based on linear filters. However, other methods can be applied, e.g. the

Bayesian approach by Hobson & McLachlan [76]. This method is based on the evaluation of the unnormalized posterior distribution $\bar{P}_r(\theta|D)$ for the parameters θ that characterize the unknown objects (such as the position, amplitude or size), given the observed data D . The unnormalized posterior probability is given in terms of the likelihood $P_r(\theta|D)$ and the prior P_r as

$$\bar{P}_r(\theta|D) \equiv P_r(D|\theta)P_r(\theta). \quad (1.2.26)$$

There are two approaches to this method. The first one is an exact approach that tries to detect all the objects present in the data simultaneously and the second, an iterative and much faster method called the ‘‘McClean Algorithm’’. In both approaches an estimation of the parameters and their errors is given. In both approaches, the parameter space that characterizes the objects is explored using Markov-Chain Monte-Carlo techniques. In this work, the authors compare the performance of both algorithms for a simple example, an image (200×200) pixels containing eight objects with a Gaussian profile and embedded on a Gaussian white noise. The signal-to-noise of the objects ranges from 0.25 to 0.5. In the first approach, the exact method, the number of objects is an additional parameter to be determined by the algorithm and all the objects are detected without false detections. However, two of the objects (which overlapped in the noiseless data) are identified as a single detection. Although the method seems to perform very well and the parameters have been estimated with a good accuracy, it is computationally demanding.

The second approach, an iterative one, tries to detect the objects one-by-one. This is going to reduce the CPU demand significantly, and the result is very similar to that of the exact method. In the considered example, the McClean algorithm provides quite similar results to the exact method, although one of the objects remains undetected. This approach can be competitive with other techniques for the detection of compact sources in future CMB experiments. However, it assumes the knowledge of the functional form of the likelihood, the prior of the parameters and the profile of the objects, which in many real situations may not be known. Moreover, other contaminants such as Galactic foregrounds would introduce additional complexity.

1.2.2 Techniques for the extraction of the Thermal SZ

The detection of the thermal SZ effect produced by clusters of galaxies in the CMB signal can be achieved with point source extraction techniques. At microwave frequencies, the clusters of galaxies appears as unresolved objects even for the highest resolution experiments. The SZ emission appear as a compact source whose shape is a

convolution of the profile of the cluster with the beam response of the instrument used for the observation. Therefore, most of the techniques developed for the detection of point sources can be used to detect the SZ effect, simply by taking into account the profile of the cluster. This has been done by Herranz et al. [68], Schulz & White [127] and Hobson & McLachlan [76], among others.

As shown in figure 1.5, the thermal SZ effect has a characteristic frequency dependence. If we have multi frequency observations, this dependence could be used to extract this emission. There are several approaches to extract the SZ signal from a map. First, there are some component separation methods that can recover simultaneously all the components, including the SZ. Second, new methods could be specifically designed to extract the SZ using multi frequency information [37, 70]. In the next subsection we will show some examples of this.

Filtering techniques

In the work by Herranz et al. [70], the authors present two techniques for the detection of SZ clusters in multi frequency maps: a combination technique and a new multi frequency filter. In both cases the profile of the cluster is assumed to be known. In the first method a linear combination of the individual frequency maps is done, using the appropriate weights to obtain the maximum amplification of the objects. Then, the combined map is filtered with a filter that takes into account the characteristics of this new map. In the second method, the individual frequency maps are filtered with a filter that takes into account the cross-correlations between frequency channels as well as the spectral dependence of the SZ effect. Then, the filtered maps are added together. In this work, the authors compared different multi frequency filters and concluded that the best one is the *Matched Multifilter* (MMF). This filter has been tested with Planck simulations, patches $12.8^\circ \times 12.8^\circ$, containing CMB, thermal and kinetic SZ effect, Galactic foregrounds (synchrotron, free-free, thermal dust and spinning dust), extragalactic point sources and instrumental noise. The authors find that the mean error in the determination of the position of the cluster is around 1 pixel, whereas the core radii are determined with an error of 0.30 pixels. Regarding the determination of the cluster amplitudes, the mean error is around 30 per cent for the brightest clusters, whereas the estimation of the weakest clusters is biased. This bias is due to the fact that for weak clusters, only those that fall on positive fluctuation of the background actually reach the detection threshold. This leads to an overestimation of their amplitude. The authors conclude that with this method it will be possible to detect ~ 10.000 clusters in 2/3 of the sky observed with Planck.

Bayesian non-parametric technique

An alternative method to detect SZ clusters in Planck has been proposed by Diego et al. [37]. In this method, the extragalactic point sources are extracted from the individual maps using the MWH. Then the map at 857 GHz is used to extract the dust component and the map at 217 GHz is used to extract the CMB. Then, a map of the Compton parameter y_c is obtained in Fourier space using the remaining frequency channels by maximizing, mode by mode, the posterior probability $P(y_c|d)$. Taking into account Bayes' theorem, this probability is given by

$$P(y_c|d) \propto P(d|y_c)P(y_c) \quad (1.2.27)$$

This maximization is done only if the likelihood function $P(d|y_c)$ and the prior $P(y_c)$ are known. Since the residuals left in the individual maps are mainly dominated by the instrumental noise, the likelihood can be approximated by a multivariate Gaussian distribution. Then, the authors find that the prior $P(y_c)$ follows approximately an exponential ($\exp(-|y_c|^2/P_{y_c})$) at each Fourier mode k , where P_{y_c} is the power spectrum of the SZ map. Taking these results into account, and after maximizing the posterior probability, the following solution for the y_c map is obtained at each mode:

$$y_c = \frac{dC^{-1}R^t}{RC^{-1}R^t + P_{y_c}^{-1}} \quad (1.2.28)$$

where d is the data, R is the response vector (this vector includes the information from the beam at each frequency and the frequency dependence of the thermal SZ effect) and C is the cross-correlation matrix of the residuals. This result is the same as the one obtained with the multi frequency Wiener filter solution from the Compton parameter y_c . The authors remark that this method does not make any assumption about the profile of the SZ clusters.

1.2.3 Techniques for the extraction of the Kinetic SZ

The kinetic SZ effect can be used to determine the peculiar velocities of individual clusters. This is a very difficult task, because this emission is one order of magnitude weaker than the thermal SZ effect, it has the same frequency dependence as the CMB and multi frequency observations can not help distinguish between them as in the thermal case. Moreover, the other diffuse galactic components and the instrumental noise makes it even more difficult. A way to approach the problem is taking into account the very strong spatial correlation between the kinetic and the thermal effects (both signals

are produced by the same cluster), and consider observations at 217 GHz, where the thermal SZ contribution is negligible. Finally, the highly non-Gaussian probability distribution from the kinetic SZ and its power spectrum are very different from the ones of the cosmological signal, and this could also be used to separate it from the CMB. There have been only a few methods that approached this complex problem [46, 60, 76]. In this work, Herranz et al. [71], the authors have used a modified matched filter on Planck simulations to study the detection of the kinematic SZ effect.

The Unbiased Matched Multifilter

A MMF can be constructed to detect the kinematic SZ effect in analogous way as for the thermal SZ effect if multi frequency observations are available. The shape of the source will be the convolution of the beam response of the instrument with the cluster profile, although the frequency dependence will now follow that of the kinetic SZ effect. The authors found that the estimation of the kinetic SZ effect (as well as the thermal one) using the MMF is biased. It can be shown that this is due to the fact that both signals have the same spatial profile. This bias is negligible for the thermal case, but not for the kinetic one. In order to correct for this bias, the authors introduced a new MMF that is unbiased, the Unbiased MMF (UMMF). The number of detections obtained with this new filter are slightly lower, but they are intrinsically unbiased. The authors tested this filter with Planck simulated data, assuming a known cluster position and profile. As expected, the strong bias has been corrected, although the error in the determination of the peculiar velocities remains very large, even for bright clusters.